Article

Signatures of chiral superconductivity in rhombohedral graphene

https://doi.org/10.1038/s41586-025-09169-7

Received: 1 September 2024

Accepted: 16 May 2025

Published online: 22 May 2025

Check for updates

Tonghang Han[1,6], Zhengguang Lu[1,2,6], Zach Hadjri[1,6], Lihan Shi[1], Zhenghan Wu[1], Wei Xu[1], Yuxuan Yao[1], Armel A. Cotten[3], Omid Sharifi Sedeh[3], Henok Weldeyesus[3], Jixiang Yang[1], Junseok Seo[1], Shenyong Ye[1], Muyang Zhou[1], Haoyang Liu[2], Gang Shi[2], Zhenqi Hua[2], Kenji Watanabe[4], Takashi Taniguchi[5], Peng Xiong[2], Dominik M. Zumbühl[3], Liang Fu[1] & Long Ju[1] ✉

Chiral superconductors are unconventional superconducting states that break time-reversal symmetry spontaneously and typically feature Cooper pairing at non-zero angular momentum. Such states may host Majorana fermions and provide an important platform for topological physics research and fault-tolerant quantum computing[1–7]. Despite intensive search and prolonged studies of several candidate systems[8–26], chiral superconductivity has remained elusive so far. Here we report the discovery of robust unconventional superconductivity in rhombohedral tetralayer and pentalayer graphene without moiré superlattice effects. We observed two superconducting states in the gate-induced flat conduction bands with T_c up to 300 mK and charge density n_e down to 2.4×10^{11} cm^{-2} in five devices. Spontaneous time-reversal-symmetry breaking (TRSB) owing to orbital motion of the electron is found and several observations indicate the chiral nature of these superconducting states, including: (1) in the superconducting state, R_{xx} shows magnetic hysteresis in varying out-of-plane magnetic field $B_\perp$—absent from all other superconductors; (2) the superconducting states are robust against in-plane magnetic field and are developed within a spin-polarized and valley-polarized quarter-metal (QM) phase; (3) the normal states show anomalous Hall signals at zero magnetic field and magnetic hysteresis. We also observed a critical $B_\perp$ of 1.4 T, higher than any graphene superconductivity, which indicates a strong-coupling superconductivity close to the Bardeen–Cooper–Schrieffer (BCS)–Bose–Einstein condensate (BEC) crossover[27]. Our observations establish a pure carbon material for the study of topological superconductivity, with the promise to explore Majorana modes and topological quantum computing.

Topological superconductivity has been conceived as new quantum states of matter, which host exotic quasiparticles that have great potential applications in quantum computing[1,2,4–7]. Chiral superconductors could host topological superconductivity with TRSB and magnetic hysteresis[2–4,6,28]. Several candidates of chiral superconductors have been investigated through a variety of experimental techniques beginning three decades ago[8–24,26]. Although signatures that are compatible with chiral superconductivity have been identified, most recent experimental reports suggest alternative pictures. For example, UTe_2 and Sr_2RuO_4 have been shown to have single-component order parameters that are incompatible with chiral superconductivity[16,29,30], and alternative origins of the observed TRSB were suggested[31]. In all of these superconductors, there has been no evidence of anomalous Hall effect or magnetic hysteresis in their charge transport, making chiral superconductivity an elusive goal to be realized.

Graphene-based two-dimensional material heterostructures have emerged as a new playground for superconductivity with unconventional ingredients. By introducing the moiré superlattice between adjacent graphene layers, or between graphene and hexagonal boron nitride (hBN), superconducting and correlated insulating states have been observed, reminiscent of the phase diagram of high-T_c superconductors (Methods). More recently, it was shown that crystalline graphene in the rhombohedral stacking order could also exhibit superconductivity in the absence of moiré effects (Methods). Rhombohedral stacked multilayer graphene hosts gate-tunable flat bands, which strongly promotes correlation effects[32,33]. As shown in Fig. 1b, the conduction band in tetralayer graphene becomes most flat when a gate-induced interlayer potential difference (between the top-most and bottom-most graphene layers) $\Delta = 90$ meV, based on our tight-binding calculation (see Methods). A similar scenario happens in pentalayer

[1]Department of Physics, Massachusetts Institute of Technology, Cambridge, MA, USA. [2]Department of Physics, Florida State University, Tallahassee, FL, USA. [3]Department of Physics, University of Basel, Basel, Switzerland. [4]Research Center for Electronic and Optical Materials, National Institute for Materials Science, Tsukuba, Japan. [5]Research Center for Materials Nanoarchitectonics, National Institute for Materials Science, Tsukuba, Japan. [6]These authors contributed equally: Tonghang Han, Zhengguang Lu, Zach Hadjri. ✉e-mail: longju@mit.edu

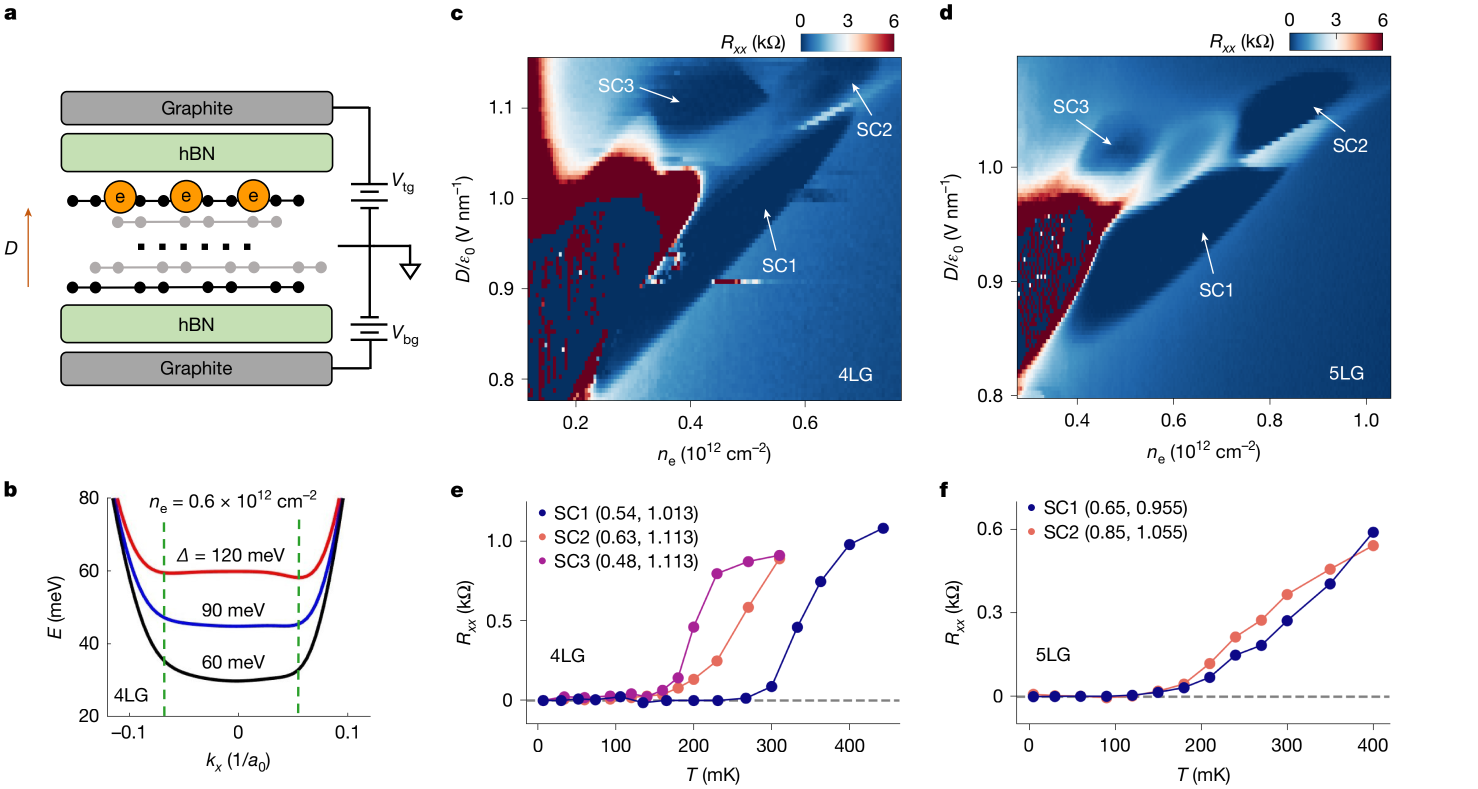

Fig. 1 | Superconductivity in the flat bands of rhombohedral tetralayer graphene device T3 and pentalayer graphene device P1. a, Illustration of the device structure, in which the tetralayer and pentalayer graphene form large twist angle with hBN to avoid the moiré superlattice effect. **b**, The dispersion of conduction band in tetralayer graphene under varying potential difference between top and bottom layer Δ, featuring a flat band bottom enclosing a charge density n_e of 0.6×10^{12} cm^{-2} per valley per spin at $\Delta = 90$ meV. **c**,**d**, Four-terminal resistance R_{xx} as a function of n_e and gate displacement field D/ε_0 taken at zero magnetic field and base temperature (7 mK at the mixing chamber) in tetralayer and pentalayer graphene, respectively. Three regions show zero R_{xx} (labelled as SC1–SC3, respectively) and superconductivity. **e**,**f**, Temperature dependence of the superconducting states in tetralayer and pentalayer graphene, respectively. The SC1–SC3 curves are taken at the labelled (n, D/ε_0) in the units of (10^{12} cm^{-2}, V nm^{-1}), respectively.

graphene. As a result, various ground states with broken spin and/or valley symmetries owing to the exchange interactions have been observed (Methods). Such states with tunable Fermi-surface topology and various spin/valley characters provide a fertile ground to search for unconventional superconductivity[34,35], including chiral superconductivity. Especially, interaction-induced valley polarization results in TRSB owing to the chirality of electron motion, whereas the valley-dependent pseudo-spin winding[32,33,36] and angular momentum[37] might facilitate high-angular-momentum pairing between electrons. The search of superconductivities in rhombohedral graphene, however, has been limited to three layers so far (Methods) and the potential of unconventional superconductivity in this system has yet to be fully explored.

Here we report the DC transport study of rhombohedral stacked tetralayer and pentalayer graphene devices. We observed superconductivity on the electron-doped side with the highest transition temperature of 300 mK. We measured three tetralayer and two pentalayer devices: device T1 is tetralayer graphene with electrons close to WSe_2, device T2 is tetralayer graphene with electrons away from WSe_2, device T3 is bare tetralayer graphene without WSe_2, devices P1 and P2 are bare pentalayer. All five devices show two unconventional superconducting states, in the absence of a detectable moiré superlattice. Several observations indicate TRSB and valley polarization in the observed superconducting states, most notably magnetic hysteresis in both the superconducting state and its corresponding normal state. These superconducting states persist to an out-of-plane magnetic field $B_\perp$ up to 1.4 T—indicating a superconducting coherence length close to the inter-electron distance—and the underlying strongly coupled superconductivity picture[27,38]. We will focus on devices T3 and P1 in the main text, as there is no WSe_2 in them and the discussion is simpler. The data from devices T1, T2 and P2 are included as Extended Data Figures (T1: Extended Data Figs. 7 and 8; T2: Extended Data Figs. 1–3; P2: Extended Data Fig. 10), in which the influence of WSe_2 will also be discussed.

Phase diagram showing superconductivity

Figure 1c shows the longitudinal resistance R_{xx} map at the nominal base temperature of 7 mK at the mixing chamber, when device T3 is electron-doped in the flat conduction band. At around $D/\varepsilon_0 = 1.1$ V nm^{-1}, three regions show vanishing resistances, as indicated by the arrows. A similar phase diagram is observed in device P1, as shown in Fig. 1d, featuring three regions of vanishing resistances, such as those in device T3. We note that SC3 in device P1 is not well developed, whereas in device P2, it is well developed (see Extended Data Fig. 10). We name these three regions SC1–SC3, as they are all superconducting states (see more data in Extended Data Figs. 4 and 9). Figure 1e,f shows the temperature dependence of R_{xx} in SC1–SC3. All three states show a transition to zero R_{xx} as the temperature is lowered. The transition temperature reaches about 300 mK for SC1 in device T3, the highest among all superconducting states in devices T3 and P1. There is another superconducting SC4 state at high electron doping observed in device T2 that is phenomenologically different from the superconductivity shown in Fig. 1c,d, especially SC1 and SC2 (see Extended Data Fig. 1).

SC1–SC3 reside at $n_e < 10^{12}$ cm^{-2}, corresponding to all of the electrons located in the flat band bottom as shown in Fig. 1b at $\Delta = 90$ meV, assuming that the electrons are of the same spin and valley characters as in a QM. At the same time, SC1–SC3 are neighboured by a highly resistive region at lower densities, which is also reminiscent of the highly

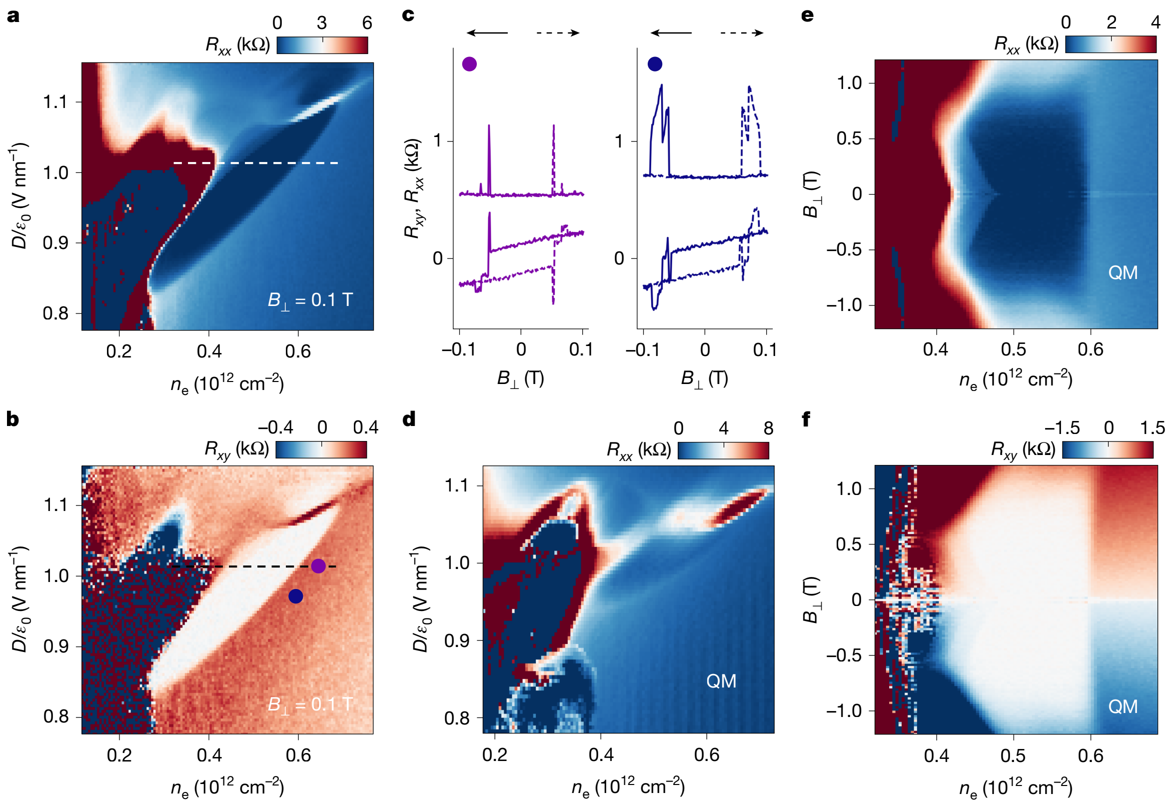

Fig. 2 | TRSB and valley polarization in the neighbouring states in the tetralayer device T3. a,**b**, R_{xx} and R_{xy} maps at 0.1 T and base temperature (7 mK at the mixing chamber), extracted by symmetrizing and antisymmetrizing the data taken at $B_\perp = \pm 0.1$ T. In **b**, SC1 (SC2) is surrounded (neighboured) by states that show anomalous Hall signals. The value of normal Hall signals at the same n_e can be seen in the high-D part of the map. **c**, R_{xy} and R_{xx} during forward (dashed curves) and backward (solid curves) scans of $B_\perp$ at the purple and blue dots in **b**. The magnetic hysteresis and anomalous Hall signal indicate valley polarization. **d**, R_{xx} map taken at $B_\perp = 1$ T. The period of quantum oscillations indicates a QM that neighbours SC1. Together with the data in **c**, this neighbouring state to SC1 is a spin-polarized and valley-polarized QM. **e**,**f**, R_{xx} and R_{xy} as a function of n_e and $B_\perp$ along the dashed line in **a** and **b** ($D/\varepsilon_0 = 1.013$ V nm^{-1}), respectively. The phase boundary between the QM and SC1 remains at the same n_e, indicating that the orbital magnetization is continuous across the boundary. The left boundary of SC1 (indicated by zero R_{xx} and R_{xy}) even expands in magnetic field, confirming its orbital magnetic nature.

resistive region in tetralayer to hexalayer rhombohedral graphene/hBN moiré superlattices (Methods). These observations of SC1–SC3 are in line with the expectation of strong electron correlation effects happening in the flat conduction band at intermediate D, as shown in Fig. 1b.

Neighbouring QM state

To better understand the superconductivities shown in Fig. 1, we first characterize the neighbouring metallic states. We use the tetralayer device T3 as an example, with the observations in the pentalayer device P1 being similar (see Extended Data Fig. 9). Figure 2a,b shows the R_{xx} and R_{xy} maps taken at $B_\perp = 0.1$ T and the base temperature, in which the SC1 and SC2 regions can be clearly seen with vanishing values in both maps. SC3 is no longer visible in these maps, indicating an out-of-plane critical magnetic field less than 0.1 T. Furthermore, Fig. 2c shows the magnetic field scans taken in the states indicated by the purple and blue dots in Fig. 2b, respectively, revealing hysteretic loops in R_{xx} and R_{xy}. Figure 2d shows the R_{xx} map taken at $B_\perp = 1$ T. The region neighbouring the high-density boundary of SC1 and the low-D boundary of SC2 shows clear quantum oscillations with a period that corresponds to that of a QM (Methods). We did not observe quantum oscillations in the regions of SC1 and SC2, possibly because of the extremely large effective mass and small cyclotron gap corresponding to the flat electron band in these regions (see Extended Data Fig. 12).

The anomalous Hall signals and magnetic hysteresis shown in Fig. 2c clearly indicate a spontaneous valley polarization and TRSB. Together with the quantum oscillation data in Fig. 2d, we conclude that SC1 and SC2 are neighboured by spin-polarized and valley-polarized QMs. The time-reversal symmetry is broken at the orbital level in these QM states and the system spontaneously chooses a chirality in its electron transport at zero magnetic field owing to the valley polarization.

After establishing that spin-polarized and valley-polarized QMs are neighbouring SC1 and SC2, we proceed to explore the evolution of the three states in magnetic field. Figure 2e,f shows the R_{xx} and R_{xy} taken along the dashed lines in Fig. 2a,b as a function of $B_\perp$. At this D, SC1 can persist to approximately 0.6 T before the R_{xx} value starts to deviate from zero. The phase boundary between SC1 and the valley-polarized QM remains at the same n_e as $B_\perp$ is increased. The left boundary even expands to lower density from $B_\perp = 0$ to 0.4 T, meaning that states in a small range of n_e become superconducting only under a non-zero $B_\perp$.

The critical magnetic field of >0.6 T in tetralayer graphene is unusually high for graphene superconductivity and the corresponding value in the pentalayer device can even reach 1.4 T. We will discuss them in detail in Fig. 5. For now, we focus on the competition between SC1 and the neighbouring states. If SC1 has zero orbital magnetization (or non-zero but smaller than that of the spin-polarized and valley-polarized QM), the range of SC1 will shrink on the application of $B_\perp$, as the energy of the QM will be lowered more than that of SC1 (Methods). The observation of SC1 holding against the neighbouring QM and even expanding implies the valley polarization and orbital magnetic nature of SC1.

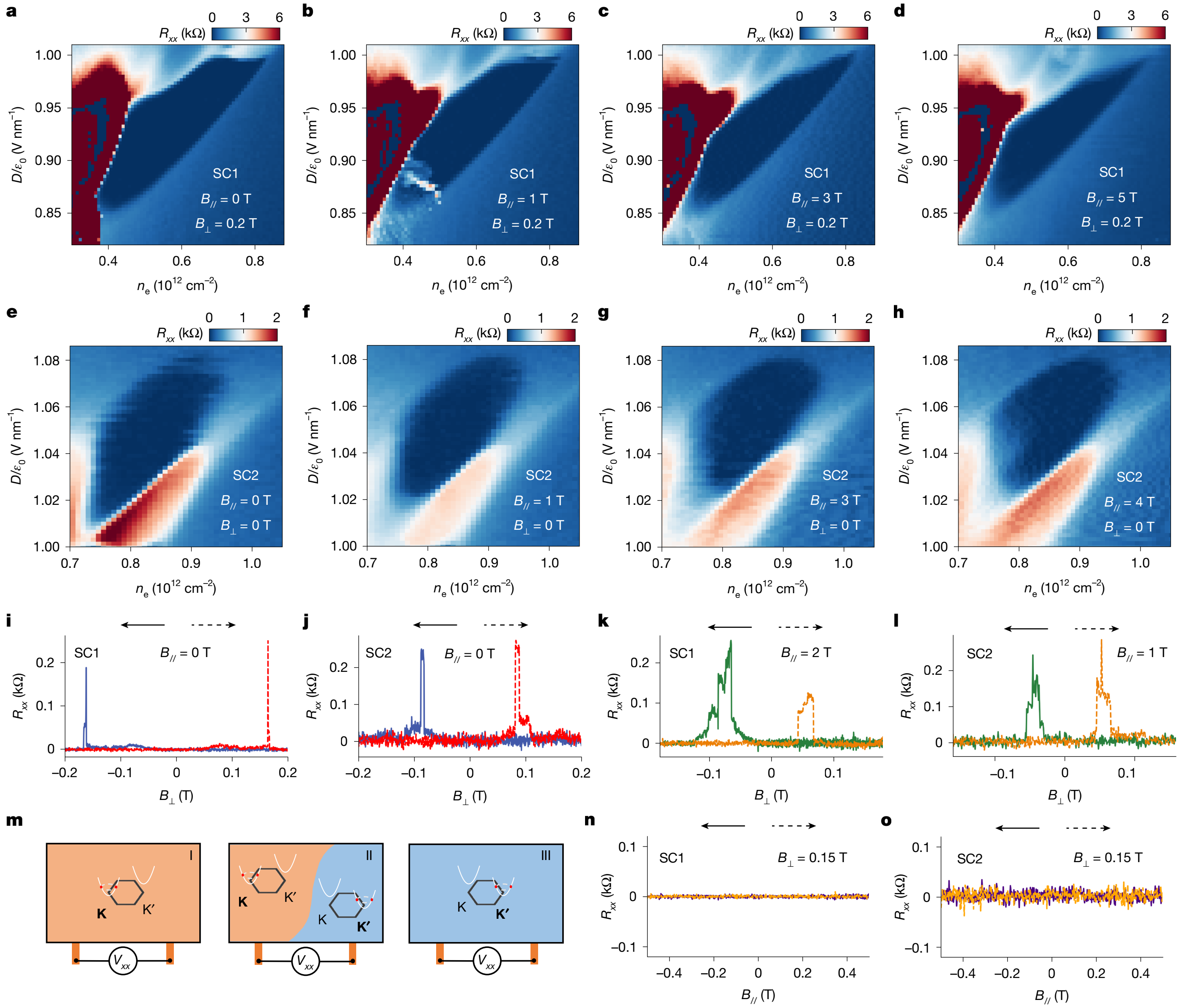

Fig. 3 | Spin and valley polarization in the superconducting states in the pentalayer device P1. a–d, n_e–D maps of R_{xx} in SC1 at in-plane magnetic field $B_{//}$ = 0, 1, 3 and 5 T, respectively (an out-of-plane magnetic field $B_{\perp}$ = 0.2 T is applied to prevent the random fluctuation of R_{xx}). **e–h**, n_e–D maps of R_{xx} in SC2 at in-plane magnetic field $B_{//}$ = 0, 1, 3 and 4 T, respectively, with an out-of-plane magnetic field $B_{\perp}$ = 0. **i**,**j**, R_{xx} during forward (dashed curves) and backward (solid curves) scans of $B_{\perp}$ at (D/ε_0 = 0.96 V nm^{-1}, n_e = 0.7 × 10^{12} cm^{-2}) and (D/ε_0 = 1.05 V nm^{-1}, n_e = 0.85 × 10^{12} cm^{-2}) in **a** and **d**, respectively. Clearly, hysteresis between two zero-resistance states can be seen in both cases, indicating a ferromagnet-like behaviour of the superconductors. **k**,**l**, R_{xx} during forward and backward scans of $B_{\perp}$ at the same states as in **i** and **j**, with $B_{//}$ = 2 T and 1 T applied, respectively. Similar hysteresis as in **i** and **j** can be seen, although the spin is fixed by the in-plane magnetic field. **m**, Illustration of the three states during the magnetic hysteresis scans in **i**–**l**, in which states I and III correspond to uniform valley-polarized domains and zero-resistance states and state II corresponds to a domain wall between oppositely valley-polarized domains between the voltage contacts and non-zero-resistance states. **n**,**o**, R_{xx} during forward and backward scans of $B_{\perp}$ at the same states as in **i** and **j**, with $B_{\perp}$ = 0.15 T applied. No hysteresis is observed in either case, in contrast to **i**–**l**.

Spin-valley-polarized superconductivity

Knowing the spin-polarized and valley-polarized QM nature of the neighbouring metallic states, next we directly scrutinize the spin and valley symmetry in SC1 and SC2. Here we use data from the pentalayer device P1 as an example. Figure 3a–d shows the n_e–D maps of R_{xx} at in-plane magnetic field $B_{//}$ = 0, 1, 3 and 5 T (an out-of-plane magnetic field $B_{\perp}$ = 0.2 T is applied to prevent the random fluctuation of R_{xx}; see Methods for discussion). Under an in-plane magnetic field, the zero resistance of superconducting state survives in most of the SC1 region that was shown at zero magnetic field. A similar observation is made for SC2, as shown in Fig. 3e–h.

The robust superconductivity in a large in-plane magnetic field indicates the spin-polarized nature of SC1 and SC2. The Pauli-limit violation ratio is already about 15 for SC1 at 5 T (see Methods) and the true Pauli-limit violation ratio is probably much larger than 15, should we increase the magnetic field to even higher values to test. The lower limits of the in-plane critical field we observed is larger than in the spin-polarized superconductivity in bilayer graphene (Methods). The spin polarization of SC1 and SC2 indicates the connection between these superconducting states and the neighbouring QM.

Figure 3i,j shows the R_{xx} under scanned $B_{\perp}$ in SC1 and SC2, respectively. Surprisingly, clear hysteresis between two zero-resistance states is observed for both superconductivities. A non-zero-resistance peak

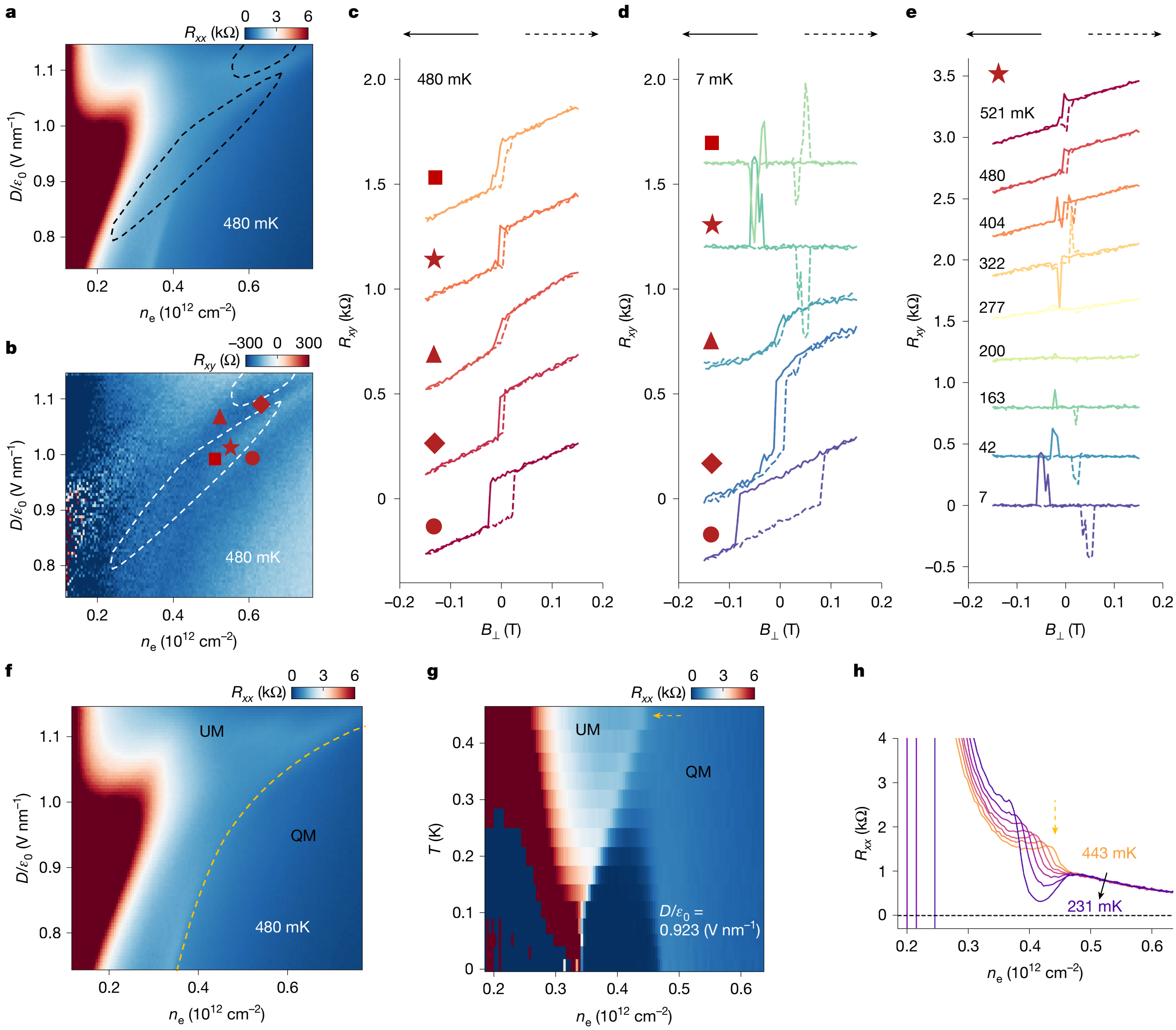

Fig. 4 | Temperature-dependent anomalous Hall effects and phase boundary in the tetralayer device T3. **a**,**b**, Symmetrized R_{xx} and antisymmetrized R_{xy} map at 0.1 T and 480 mK, above the critical temperatures of SC1 and SC2. The dashed curves outline the boundaries of SC1 and SC2, inside which clear anomalous Hall signals can be seen in the normal states in **b**. **c**,**d**, Magnetic field scans of R_{xy} at the square, star, triangle, diamond and dot positions in **b** at 480 and 7 mK, respectively. Clear hysteresis can be seen in both of the states surrounding SC1, as well as in the SC1 region. Such an anomalous Hall signal indicates TRSB owing to the orbital degree of freedom, which is absent in any previously reported superconductors. **e**, Temperature-dependent R_{xy} hysteresis at the star position. At 277–521 mK, non-zero value of R_{xy} at $B = 0$ T and a linear R_{xy} versus B (the normal Hall signal) can be seen. Below 277 mK, these components disappear as a result of the superconductivity, whereas clear hysteresis can still be seen. **f**, The same R_{xx} map as in **a**, highlighting (by the orange dashed curve) the phase boundary between the spin-polarized and valley-polarized QM and an UM. **g**, Temperature-dependent R_{xx} linecut at $D/\varepsilon_0 = 0.923$ V nm^{-1}, at which the QM–UM phase boundary gradually shifts as T is lowered. The SC1 state develops to the right of the boundary, indicating the QM as the parent state of SC1. **h**, Linecuts from **g**, showing the QM–UM phase boundary as a kink in R_{xx}, which shifts to lower n_e as T is lowered.

appears during the scanning, the magnetic field at which shows a hysteresis between forward and backward scans. Furthermore, such a non-zero-resistance peak between zero-resistance states and the hysteresis behaviour are observed even when a large in-plane magnetic field $B_{//}$ is applied, as shown in Fig. 3k,l.

The magnetic hysteresis of resistance in a superconducting state is highly unusual and distinct from all other superconductors: ferromagnetic superconductors show magnetic hysteresis in their optical responses but not in resistance directly[39]; magnetic hysteresis in resistance owing to vortex-array melting happen between the superconducting and metallic states[40], rather than between two superconducting states. The observations in Fig. 3i–l suggest the orbital magnetic nature of SC1 and SC2. This is illustrated in Fig. 3m: the two zero-resistance states at large $B_\perp$ field correspond to a single (and opposite) valley-polarized domain between the voltage contacts in the device, whereas the non-zero resistance during scanning happens when a domain wall separates opposite-valley-polarized domains. This domain is expected to be resistive, as the tunnelling of Cooper pair through it does not conserve momentum. The domain is flipped as a result of the coupling of valley-orbital magnetization and the out-of-plane magnetic field—a mechanism similar to that which induces the hysteresis shown in Fig. 2c. The possibility of domain flipping owing

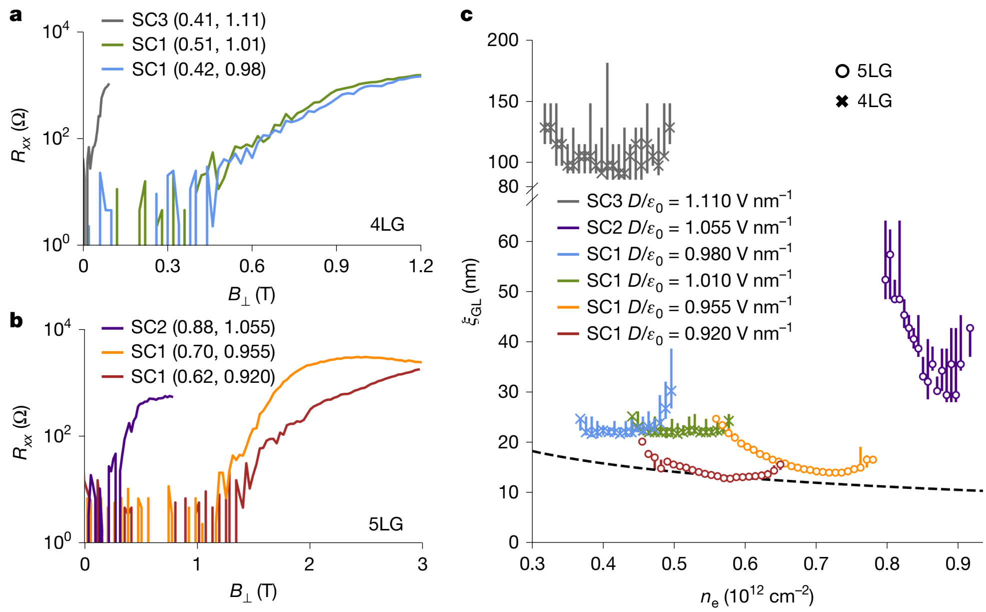

Fig. 5 | Superconductivity close to the BCS–BEC crossover. a,b, Dependence of resistances in SC1–SC3 on $B_\perp$ at 7 mK in the tetralayer device T3 and pentalayer device P1, respectively. The curves were taken at (n, D/ε_0) labelled in the figure in the units of (10^{12} cm^{-2}, V nm^{-1}), respectively. **c**, Coherence length ξ_{GL} as a function of charge density in SC1–SC3. Here the critical magnetic field and its uncertainties are defined as the field at 10% and field range between 5% and 15% of the normal state resistance, respectively. The dashed lines represent the inter-particle distance derived from the corresponding n_e. The ξ_{GL} in SC1 in the pentalayer device is close to the inter-particle distance, indicating strongly coupled Cooper pairing that is close to the BEC–BCS crossover but still mainly on the BCS side.

to coupling to the spin magnetization is ruled out in two ways: (1) in Fig. 3k,l, the spin is always locked to the in-plane direction during scanning owing to the much larger $B_{//}$ field than $B_\perp$ field; (2) when the valley polarization is fixed by a $B_\perp$ field, scanning the $B_{//}$ field in a large range does not induce any non-zero-resistance state or hysteresis, as shown in Fig. 3n,o. These observations strongly suggest the similarity and connection between the spin-valley-polarized QM and SC1 and SC2 (see Extended Data Fig. 5).

Temperature-dependent phase evolution

Another approach to understand the SC1 and SC2 as well as their relation with the neighbouring QM is to explore the corresponding normal states. Here we focus on data from the tetralayer device T3 for the most complete characterization. The behaviours in other devices are qualitatively the same (see Extended Data Figs. 3 and 9 for examples). Figure 4a,b shows the symmetrized R_{xx} and antisymmetrized R_{xy} maps, respectively, at $B_\perp$ = 0.1 T and T = 480 mK. The zero resistances in both SC1 and SC2 are replaced by values that are around 1–2 kΩ. In the Hall resistance map (Fig. 4b), anomalous Hall signals of roughly 100 Ω are distributed in a region that overlaps with the SC1 and SC2 regions (outlined by the dashed oval-shaped curves). These anomalous Hall signals are confirmed by Fig. 4c, in which the R_{xy} at scanned magnetic fields are shown for representative n_e–D combinations both within SC1 and in surrounding states (corresponding to the five symbols in Fig. 4b). Such magnetic hysteresis persists to 7 mK while R_{xy} is zero in SC1 except for at the coercive fields, as shown in Fig. 4d. Figure 4e shows the evolution of R_{xy} hysteresis as a function of temperature at the star position.

These observations suggest that the TRSB and valley polarization already exist in the normal states of superconducting SC1 and SC2 states. To our knowledge, this is the first time that an anomalous Hall signal at zero magnetic field and magnetic hysteresis behaviour are observed in the normal state of a superconductor, except for in hybrid systems, in which superconductivity and ferromagnetism coexist[39,41–43]. These features are inherited by the electrons when they become superconducting at below the transition temperature. The Hall angles in these anomalous Hall states are large, corresponding to $\tan\theta_H = \frac{R_{xy}}{R_{xx}}$ approximately up to 0.1, which is typical for QM states in crystalline rhombohedral graphene devices (Methods).

We note that there is a clear boundary intercepting the SC1 region in Fig. 4a, which corresponds to a sudden change of R_{xx}. This boundary is highlighted by the orange dashed curve in Fig. 4f. At a specific displacement field (D/ε_0 = 0.923 V nm^{-1} for example, as shown in Fig. 4g), this phase boundary and kink in R_{xx} gradually shift to lower n_e during cooling down. At about 250 mK, the SC1 dome starts to develop in the region that is on the higher density side of this phase boundary. Figure 4h shows linecuts at varying temperatures that highlight the kink and its temperature-dependent evolution.

By performing quantum oscillation measurements, we determine the higher density side of this boundary to be the spin-polarized and valley-polarized QM. It is hard to determine the Fermi surface topology of the lower density side owing to the lack of clear quantum oscillations (we thus name it ‘undetermined metal’ or UM), whereas one possibility is a metal state with annular Fermi surface and full spin and valley polarizations (see Extended Data Fig. 6 for details). Although at 480 mK the QM–UM phase boundary intercepts the SC1 region, the same phase boundary gradually shifts to lower n_e and eventually encloses the entire SC1 region into the QM phase. This observation indicates that the SC1 state develops from the spin-polarized and valley-polarized QM parent state.

Strong coupling of Cooper pairing

Last, we explore the out-of-plane magnetic-field dependence of SC1–SC3 in greater detail. Figure 5a,b shows the R_{xx} in SC1–SC3 states as a function of $B_\perp$ in the tetralayer and pentalayer devices, respectively. In both cases, we can see that R_{xx} deviates from zero as $B_\perp$ is increased. We define the critical magnetic field $B_{\perp,c}$ as the field when R_{xx} reaches 10% of the normal state resistance and its uncertainty as the field range between 5% and 15% (see Extended Data Fig. 9) and extract the phenomenological Ginzburg–Landau superconducting coherence length as $\xi_{GL} = \left(\frac{\Phi_0}{2\pi B_{\perp,c}}\right)^{\frac{1}{2}}$, in which $\Phi_0 = \frac{h}{2e}$ is the superconducting magnetic flux quantum. Notably, R_{xx} in SC1 in the pentalayer device remains within the noise level until $B_{\perp} = 1.4$ T. Figure 5c summarizes ξ_{GL} as a function of n_e for SC1–SC3 at representative displacement fields. As a reference, we plot the inter-electron distance $d_{particle} = n_e^{-1/2}$ determined by the charge density n_e (ref. 38). The coherence length in SC3 is well above the inter-electron distance. However, the coherence length in SC1 and SC2 are much closer to the latter, especially SC1 in the pentalayer device.

The observations show that SC1 is very unusual in that the electrons have a much stronger coupling strength. SC1 is already close to the BCS–BEC crossover[27], although it still mainly resides on the BCS side. We note that the critical magnetic field $B_{\perp,c}$ observed in our pentalayer device is higher than any graphene-based superconductors, crystalline or twisted. Compared with the superconducting state in twisted trilayer graphene[38], the T_c of SC1 in our experiment is more than ten times lower, but the electron density at which superconductivity is observed is similar, whereas the critical magnetic field $B_{\perp,c}$ is 2–3 times higher.

Discussion

To summarize, we observed two superconducting states SC1 and SC2 that exhibit unusual properties: (1) magnetic hysteresis and orbital magnetism in the superconducting states; (2) SC1 develops within a spin-polarized and valley-polarized QM phase and is robust against the remaining QM state under an out-of-plane magnetic field; (3) the non-zero anomalous Hall signals at zero magnetic field and clear magnetic hysteresis at temperatures above T_c. These observations clearly suggest unconventional superconductivity that is distinct from any existing superconductors. These observations also suggest spontaneous TRSB at the orbital level in the superconducting states, which is the defining feature of chiral superconductivity[2–4,6].

Microscopically, our observations indicate a spin-symmetry-broken and valley-symmetry-broken parent state of superconductivity in SC1 and a valley-symmetry-broken parent state of SC2. In SC1, the parent state is a fully spin-polarized and valley-polarized QM, which has only one pocket at the Fermi level. In SC2, the parent state is probably a metal state with an annular Fermi surface, which might even have occupations in two different-sized pockets located in opposite valleys (which may have full or partial spin/valley polarization). In the QM case, Cooper pairing occurs within the same spin states in a single valley, which must have odd angular momentum owing to the Pauli exclusion principle, for example, p-wave or f-wave. Owing to the presence of Berry curvature in the valley-polarized state as evidenced by the anomalous Hall effect above T_c, we expect that the complex-valued chiral order parameter such as $p + ip$ is favoured over the real order parameter, such as p_x. Such chiral superconductors with a single non-degenerate Fermi pocket in two dimensions may be topologically nontrivial and host localized Majorana modes in the vortex core and chiral Majorana fermions at the boundary[2]. We also note that intravalley pairing leads to a large Cooper pair momentum, thus realizing a finite-momentum superconductor[24,25,44–46]. We note that, in roughly the same n_e–D range hosting SC1–SC3, tetralayer to hexalayer rhombohedral graphene/hBN moiré superlattice devices show fractional quantum anomalous Hall effects that are hosted by a valley-polarized and spin-polarized topological flat band (Methods).

Our experiment demonstrates a new platform based on simple crystalline graphene for exploring topological superconductivity with local and chiral Majorana zero modes[1–7]. To understand the superconducting ground states that we have observed, future experiments may be performed in several exciting directions: (1) directly investigating the TRSB and the orbital magnetism in the superconducting state by using Kerr rotation optical spectroscopy[47] or scanning SQUID[43,48,49]; (2) determining the superconducting gap symmetry by measuring the Fraunhofer pattern of in-plane Josephson junctions[50,51] or Little–Parks effect[52]; (3) characterizing the distribution of supercurrent in magnetic field[53,54] and/or by directly imaging the possible persistent edge current by scanning SQUID[48]; (4) testing quantized thermal conductance of possible Majorana chiral modes on the edges[55]. Our experiment opens up new directions in superconductivity and electron topology physics and could pave the way to non-abelian quasi-particle engineering for topologically protected quantum computation applications.

Online content

Any methods, additional references, Nature Portfolio reporting summaries, source data, extended data, supplementary information, acknowledgements, peer review information; details of author contributions and competing interests; and statements of data and code availability are available at https://doi.org/10.1038/s41586-025-09169-7.

1. Sato, M. & Ando, Y. Topological superconductors: a review. *Rep. Prog. Phys.* **80**, 076501 (2017).
2. Read, N. & Green, D. Paired states of fermions in two dimensions with breaking of parity and time-reversal symmetries and the fractional quantum Hall effect. *Phys. Rev. B* **61**, 10267–10297 (2000).
3. Kallin, C. & Berlinsky, J. Chiral superconductors. *Rep. Prog. Phys.* **79**, 054502 (2016).
4. Qi, X.-L. & Zhang, S. C. Topological insulators and superconductors. *Rev. Mod. Phys.* **83**, 1057–1110 (2011).
5. Kitaev, A. Periodic table for topological insulators and superconductors. *AIP Conf. Proc.* **1134**, 22–30 (2009).
6. Nayak, C., Simon, S. H., Stern, A., Freedman, M. & Das Sarma, S. Non-Abelian anyons and topological quantum computation. *Rev. Mod. Phys.* **80**, 1083–1159 (2008).
7. Schnyder, A. P., Ryu, S., Furusaki, A. & Ludwig, A. W. W. Classification of topological insulators and superconductors in three spatial dimensions. *Phys. Rev. B* **78**, 195125 (2008).
8. Maeno, Y. et al. Superconductivity in a layered perovskite without copper. *Nature* **372**, 532–534 (1994).
9. Ghosh, S. et al. Thermodynamic evidence for a two-component superconducting order parameter in Sr_2RuO_4. *Nat. Phys.* **17**, 199–204 (2021).
10. Saxena, S. Superconductivity on the border of itinerant-electron ferromagnetism in UGe_2. *Nature* **406**, 587–592 (2000).
11. Stewart, G. R., Fisk, Z., Willis, J. O. & Smith, J. L. Possibility of coexistence of bulk superconductivity and spin fluctuations in UPt_3. *Phys. Rev. Lett.* **52**, 679–682 (1984).
12. Aoki, D. Coexistence of superconductivity and ferromagnetism in URhGe. *Nature* **413**, 613–616 (2001).
13. Ran, S. et al. Nearly ferromagnetic spin-triplet superconductivity. *Science* **365**, 684–687 (2019).
14. Hayes, I. M. et al. Multicomponent superconducting order parameter in UTe_2. *Science* **373**, 797–801 (2021).
15. Jiao, L. et al. Chiral superconductivity in heavy-fermion metal UTe_2. *Nature* **579**, 523–527 (2020).
16. Theuss, F. et al. Single-component superconductivity in UTe_2 at ambient pressure. *Nat. Phys.* **20**, 1124–1130 (2024).
17. Nandkishore, R., Levitov, L. S. & Chubukov, A. V. Chiral superconductivity from repulsive interactions in doped graphene. *Nat. Phys.* **8**, 158–163 (2012).
18. Ming, F. et al. Evidence for chiral superconductivity on a silicon surface. *Nat. Phys.* **19**, 500–506 (2023).
19. Wan, Z. et al. Unconventional superconductivity in chiral molecule–TaS_2 hybrid superlattices. *Nature* **632**, 69–74 (2024).
20. Li, Z. et al. Observation of odd-parity superconductivity in UTe_2. *Proc. Natl Acad. Sci.* **122**, e2419734122 (2025).
21. Mielke, C. et al. Time-reversal symmetry-breaking charge order in a kagome superconductor. *Nature* **602**, 245–250 (2022).
22. Yin, J. X., Lian, B. & Hasan, M. Z. Topological kagome magnets and superconductors. *Nature* **612**, 647–657 (2022).
23. Le, T. et al. Superconducting diode effect and interference patterns in kagome CsV_3Sb_5. *Nature* **630**, 64–69 (2024).
24. Hsu, Y. T., Vaezi, A., Fischer, M. H. & Kim, E. A. Topological superconductivity in monolayer transition metal dichalcogenides. *Nat. Commun.* **8**, 14985 (2017).
25. Murshed, S. A., Szabó, A. L. & Roy, B. Nodal pair-density-waves from quarter-metal in crystalline graphene multilayers. Preprint at https://arxiv.org/abs/2210.15660 (2022).
26. Deng, H. et al. Evidence for time-reversal symmetry-breaking kagome superconductivity. *Nat. Mater.* **23**, 1639–1644 (2024).
27. Randeria, M. & Taylor, E. Crossover from Bardeen-Cooper-Schrieffer to Bose-Einstein condensation and the unitary Fermi gas. *Annu. Rev. Condens. Matter Phys.* **5**, 209–232 (2014).
28. Cheng, M., Sun, K., Galitski, V. & Das Sarma, S. Stable topological superconductivity in a family of two-dimensional fermion models. *Phys. Rev. B Condens. Matter Mater. Phys.* **81**, 024504 (2010).
29. Li, Y. S. et al. High-sensitivity heat-capacity measurements on Sr_2RuO_4 under uniaxial pressure. *Proc. Natl Acad. Sci. USA* **118**, e2020492118 (2021).
30. Pustogow, A. et al. Constraints on the superconducting order parameter in Sr_2RuO_4 from oxygen-17 nuclear magnetic resonance. *Nature* **574**, 72–75 (2019).
31. Willa, R., Hecker, M., Fernandes, R. M. & Schmalian, J. Inhomogeneous time-reversal symmetry breaking in Sr_2RuO_4. *Phys. Rev. B* **104**, 024511 (2021).
32. Min, H. & MacDonald, A. H. Electronic structure of multilayer graphene. *Prog. Theor. Phys. Suppl.* **176**, 227–252 (2008).

33. Koshino, M. & McCann, E. Trigonal warping and Berry's phase $N\pi$ in ABC-stacked multilayer graphene. *Phys. Rev. B* **80**, 165409 (2009).
34. Ghazaryan, A., Holder, T., Berg, E. & Serbyn, M. Multilayer graphenes as a platform for interaction-driven physics and topological superconductivity. *Phys. Rev. B* **107**, 104502 (2023).
35. Viñas Boström, E. et al. Phonon-mediated unconventional superconductivity in rhombohedral stacked multilayer graphene. *NPJ Comput. Mater.* **10**, 163 (2024).
36. Castro Neto, A. H., Guinea, F., Peres, N. M. R., Novoselov, K. S. & Geim, A. K. The electronic properties of graphene. *Rev. Mod. Phys.* **81**, 109–162 (2009).
37. Cao, T., Wu, M. & Louie, S. G. Unifying optical selection rules for excitons in two dimensions: band topology and winding numbers. *Phys. Rev. Lett.* **120**, 087402 (2018).
38. Park, J. M., Cao, Y., Watanabe, K., Taniguchi, T. & Jarillo-Herrero, P. Tunable strongly coupled superconductivity in magic-angle twisted trilayer graphene. *Nature* **590**, 249–255 (2021).
39. Yi, H. et al. Interface-induced superconductivity in magnetic topological insulators. *Science* **383**, 634–639 (2024).
40. Safar, H. et al. Experimental evidence for a first-order vortex-lattice-melting transition in untwinned, single crystal $YBa_2Cu_3O_7$. *Phys. Rev. Lett.* **69**, 824 (1992).
41. Hu, Y., Meng, F., Lei, H., Xue, Q.-K. & Zhang, D. Possible spin-polarized Cooper pairing in high temperature FeSe superconductor. Preprint at https://arxiv.org/abs/2405.10482 (2024).
42. Ma, L. et al. Electric-field-controlled superconductor–ferromagnetic insulator transition. *Sci. Bull.* **64**, 653–658 (2019).
43. Bert, J. A. et al. Direct imaging of the coexistence of ferromagnetism and superconductivity at the $LaAlO_3/SrTiO_3$ interface. *Nat. Phys.* **7**, 767–771 (2011).
44. Fulde, P. & Ferrell, R. A. Superconductivity in a strong spin-exchange field. *Phys. Rev.* **135**, A550 (1964).
45. Larkin, A. I. & Ovchinnikov, Y. N. Inhomogeneous state of superconductors. *Sov. Phys. JETP* **20**, 762–769 (1965).
46. Casalbuoni, R. & Nardulli, G. Inhomogeneous superconductivity in condensed matter and QCD. *Rev. Mod. Phys.* **76**, 263 (2004).
47. Charbonneau, P. et al. Polar Kerr effect as probe for time-reversal symmetry breaking in unconventional superconductors. *New J. Phys.* **11**, 055060 (2009).
48. Uri, A. et al. Nanoscale imaging of equilibrium quantum Hall edge currents and of the magnetic monopole response in graphene. *Nat. Phys.* **16**, 164–170 (2019).
49. Tschirhart, C. L. et al. Imaging orbital ferromagnetism in a moiré Chern insulator. *Science* **372**, 1323–1327 (2021).
50. Wollman, D. A., Van Harlingen, D. J., Lee, W. C., Ginsberg, D. M. & Leggett, A. J. Experimental determination of the superconducting pairing state in YBCO from the phase coherence of YBCO-Pb dc SQUIDs. *Phys. Rev. Lett.* **71**, 2134 (1993).
51. Tsuei, C. C. & Kirtley, J. R. Pairing symmetry in cuprate superconductors. *Rev. Mod. Phys.* **72**, 969–1016 (2000).
52. Li, Y., Xu, X., Lee, M. H., Chu, M. W. & Chien, C. L. Observation of half-quantum flux in the unconventional superconductor β-Bi_2Pd. *Science* **366**, 238–241 (2019).
53. Hart, S. et al. Induced superconductivity in the quantum spin Hall edge. *Nat. Phys.* **10**, 638–643 (2014).
54. Wang, W. et al. Evidence for an edge supercurrent in the Weyl superconductor $MoTe_2$. *Science* **368**, 534–537 (2020).
55. Kasahara, Y. et al. Majorana quantization and half-integer thermal quantum Hall effect in a Kitaev spin liquid. *Nature* **559**, 227–231 (2018).

Publisher's note Springer Nature remains neutral with regard to jurisdictional claims in published maps and institutional affiliations.

Methods

Device fabrication

The graphene, WSe_2 (from HQ Graphene) and hBN flakes were prepared by mechanical exfoliation onto SiO_2/Si substrates. The rhombohedral domains of tetralayer and pentalayer graphene were identified and confirmed using an infrared camera[56], near-field infrared microscopy and Raman spectroscopy and isolated by cutting with a femtosecond laser. The van der Waals heterostructure was made following a dry-transfer procedure. We picked up the top hBN, graphite, middle hBN, WSe_2 and the tetralayer (pentalayer) graphene using polypropylene carbonate film and landed it on a prepared bottom stack consisting of a hBN and graphite bottom gate. We misaligned the long straight edge of the graphene and hBN flakes to avoid forming a large moiré superlattice. The device was then etched into a multiterminal structure using standard e-beam lithography and reactive-ion etching. We deposited Cr–Au for electrical connections to the source, drain and gate electrodes.

Transport measurement

The devices were measured mainly in a Bluefors LD250 dilution refrigerator at MIT with a lowest electronic temperature of around 40 mK. Stanford Research Systems SR830 lock-in amplifiers and SP1004 voltage preamplifiers from Basel Precision Instruments were used to measure the longitudinal and Hall resistance R_{xx} and R_{xy} with an AC frequency at 17.77 Hz. The DC and AC currents are generated by a Keysight 33210A function generator through a 100-MΩ resistor. The AC current excitation was limited to be below 0.5 nA. All measurement lines are filtered by the Basel Precision Instruments microwave filter MFT25. Device T1 was also measured in an Oxford dilution refrigerator at Florida State University. Device P1 was also measured at the University of Basel in a Leiden MNK126-700 dilution refrigerator with a base temperature of about 5 mK. An MFLI Zurich Instruments lock-in amplifier (at 17.77 Hz) modulated the AC signal on the DC, followed by a 1-MΩ resistor to fix the current. Basel Precision Instruments preamps were used to measure differential currents and voltages. Keithley 2400 source meters were used to apply top-gate and bottom-gate voltages. Top-gate voltage V_t and bottom-gate voltage V_b are swept to adjust doping density $n_e = (C_t V_t + C_b V_b)/e$ and displacement field $D/\varepsilon_0 = (C_t V_t - C_b V_b)/2$, in which C_t and C_b are the top-gate and bottom-gate capacitance per area calculated from the Landau fan diagram.

Tight-binding model calculation

The single-particle band structure of the rhombohedral stacked tetralayer graphene is calculated from an effective eight-band Slonczewski–Weiss–McClure type tight-binding model

$$H=\begin{pmatrix} u/2 & \upsilon_0\pi^\dagger & \upsilon_4\pi^\dagger & \upsilon_3\pi & 0 & \gamma_2/2 & 0 & 0\\ \upsilon_0\pi & u/2 & \gamma_1 & \upsilon_4\pi^\dagger & 0 & 0 & 0 & 0\\ \upsilon_4\pi & \gamma_1 & u/6 & \upsilon_0\pi^\dagger & \upsilon_4\pi^\dagger & \upsilon_3\pi & 0 & \gamma_2/2\\ \upsilon_3\pi^\dagger & \upsilon_4\pi & \upsilon_0\pi & u/6 & \gamma_1 & \upsilon_4\pi^\dagger & 0 & 0\\ 0 & 0 & \upsilon_4\pi & \gamma_1 & -u/6 & \upsilon_0\pi^\dagger & \upsilon_4\pi^\dagger & \upsilon_3\pi\\ \gamma_2/2 & 0 & \upsilon_3\pi^\dagger & \upsilon_4\pi & \upsilon_0\pi & -u/6 & \gamma_1 & \upsilon_4\pi^\dagger\\ 0 & 0 & 0 & 0 & \upsilon_4\pi & \gamma_1 & -u/2 & \upsilon_0\pi^\dagger\\ 0 & 0 & \gamma_2/2 & 0 & \upsilon_3\pi^\dagger & \upsilon_4\pi & \upsilon_0\pi & -u/2 \end{pmatrix}$$

in the basis of (A1, B1, A2, B2, A3, B3, A4, B4), as in the trilayer case[57,58]. Here $\upsilon_i = \sqrt{3}\,a_0\gamma_i/2\hbar$ and $a_0 = 0.246$ nm. The parameters we used are: $\gamma_0 = 3.25$ eV, $\gamma_1 = 0.400$ eV, $\gamma_2 = -0.0166$ eV, $\gamma_3 = -0.293$ eV and $\gamma_4 = -0.144$ eV. A perpendicular displacement field can introduce a screened potential difference between the top and bottom layers, denoted by Δ. The band structure for rhombohedral pentalayer graphene is calculated using the same parameters with a ten-band model.

The estimation of effective mass in this case is complex owing to the trigonally warped non-parabolic band structure. The effective mass is highly dependent on the density and electric field. We define an averaged effective mass by calculating the density and average kinetic energy[59]

$$n=\int_{E_m}^{E_F}\frac{d^2\mathbf{k}}{(2\pi)^2},\quad W=\frac{1}{n}\int_{E_m}^{E_F}\frac{d^2\mathbf{k}}{(2\pi)^2}(E(\mathbf{k})-E_m)$$

in which E_F and E_m denote the Fermi energy and the conduction band minimum, respectively. $E(\mathbf{k})$ is the band energy at momentum $\mathbf{k}$. Then we compare this with a parabolic band with the same density n and same average kinetic energy W and get the effective mass. We plot the effective mass m^* and Fermi energy E_F as a function of density when $\Delta = 90$ meV (Extended Data Fig. 12a) and when $n_e = 0.5\times10^{12}$ cm^{-2} (Extended Data Fig. 12b), near which superconductivity appears. We also plot the effective mass m^* and Fermi energy E_F as a function of density when $\Delta = 63$ meV (Extended Data Fig. 12c) and when $n_e = 0.6\times10^{12}$ cm^{-2} (Extended Data Fig. 12d). The calculation assumes that there is only one single-valley polarized band, suggested by the experiment.

Previous experimental efforts on graphene-based two-dimensional material heterostructures

Introducing the moiré superlattice between adjacent graphene layers[60–62], or between graphene and hBN[63], has led to observations of superconducting and correlated insulating states, resembling the phase diagrams of high-T_c superconductors. More recently, it was shown that crystalline graphene with the rhombohedral stacking order could also exhibit superconductivity in the absence of moiré effects[64–72]. Rhombohedral stacked multilayer graphene hosts gate-tunable flat bands, which strongly promotes correlation effects, resulting in diverse ground states characterized by broken spin and/or valley symmetries arising from exchange interactions[73–78]. By introducing moiré potential through an adjacent hBN layer and under the application of a perpendicular electric field, multilayer rhombohedral graphene/hBN moiré can host integer and fractional quantum anomalous Hall effects[56,79,80], happening roughly in the same (n_e, D) range as the superconducting state SC1 reported in this work, in which the moiré effect is negligible.

Devices T1, T2 and P2

Device T2 has a monolayer WSe_2 on top of the tetralayer graphene. Device T1 has a bilayer WSe_2 beneath the tetralayer graphene. Device P2 is a bare pentalayer graphene without WSe_2. Owing to the contact geometry, we can reliably measure the superconducting phases only when the electrons in the conduction band are pushed towards the WSe_2 in device T1 and when electrons in the conduction band are pushed away from WSe_2 in device T2.

The general phase diagram of devices T1 and T2 are similar to that of device T3. In devices T1, SC1, SC2 and SC3 are observed (Extended Data Figs. 7 and 8). At $B = 0$ T, both SC1 and SC2 show fluctuations when scanning the gate voltages, whereas SC3 does not. At $B_\perp = 0.1$ T, SC3 is destroyed, whereas SC1 and SC2 remain. Magnetic field scans reveal anomalous Hall signals surrounding SC1 (Extended Data Fig. 7). There is also magnetic hysteresis inside SC1. SC1 survives up to $B_\perp \approx 0.8$ T and the phase boundary between SC1 and the higher-density QM remains unchanged or even slightly leans towards the QM (Extended Data Fig. 8). SC2 survives up to about 0.4 T (Extended Data Fig. 8).

In device T2, we observed SC1, SC2 and SC3, as well as an extra SC4 (Extended Data Fig. 1). The phase boundary of QM shifts to lower density as the temperature decreases and SC1 emerges from the QM. Such behaviour was observed in all three devices (Extended Data Fig. 11).

Although sharing similar qualitative behaviours, the three devices are quantitatively different. For example, the $T_{BKT,SC1}$ for devices T1, T2 and T3 are 160 mK, 210 mK and 300 mK, respectively. The difference could originate from the existence of WSe_2 and also the device-quality variations.

The general phase diagram and behaviours of devices P1 (Extended Data Fig. 9) and P2 (Extended Data Fig. 10) are similar.

Fluctuations in resistance maps and time domain

When measuring R_{xx} maps at close to zero magnetic field, we often observe fluctuations in the SC1, SC2 and the neighbouring QM states. This is a universal observation (see Fig. 1 for T3, Extended Data Fig. 1 for T2 and Extended Data Fig. 7 for T1). The frequency of such fluctuations, however, depends on the details of the specific device and measurement, such as the coercive magnetic field (less when the coercive field is bigger) and the cooling history (less when field-cooled). When fixing the n_e and D, it is also possible to see fluctuations of R_{xx} as a function of time, such as shown in Extended Data Fig. 1j. The fluctuations in the QM state we observed have also been observed in previous experiments in rhombohedral trilayer graphene and were attributed to flipping of the valley polarization and orbital magnetism[64]. The fluctuations we observed in the SC1 and SC2 states, however, have not been reported in any superconductors. We think that the origin of these fluctuations in the superconducting states is also the flipping of valley polarization and orbital magnetism.

Quantum oscillations and fermiology of the neighbouring states of SC1 and SC2

Although the spin-polarized and valley-polarized QM are clearly established by the quantum oscillation data and the valley-orbital-magnetic hysteresis, the Fermi surface topology in the UM state in Fig. 4f is much less clear. This can be seen from Fig. 2 and Extended Data Fig. 9, in which no clear quantum oscillations can be observed in the region to the lower density side of the QM–UM phase boundary.

Extended Data Fig. 6b,c shows the Landau fan at $D/\varepsilon_0 = 1.123$ V nm^{-1} and the corresponding fast Fourier transform spectra. Quantum oscillations can be seen starting at about 1.5 T in the first panel and a diagonal feature can be seen in the second panel. The diagonal feature is similar to that observed in the annular Fermi-surfaced metal state in rhombohedral trilayer graphene[73], which has a frequency above 1. The corresponding low-frequency feature observed in trilayer graphene, however, is missing from our data. Admittedly, the low-frequency component of fast Fourier transform is usually more difficult to extract. This is especially true in our case, owing to the large effective mass in the flat conduction band. On the basis of these observations, we can only speculate the UM state to be possibly a spin-polarized and valley-polarized QM with an annular Fermi surface. This undetermined nature of the UM state (which is to the lower density side of the QM–UM phase boundary), however, does not affect visualizing the temperature dependence of phase evolutions and our conclusion of SC1 stemming from a spin-polarized and valley-polarized QM parent state.

Extraction of coherence length

We define the critical magnetic field $B_{\perp,c}$ as the field when the R_{xx} reaches 10% of the normal state resistance and its uncertainty as the field range between 5% and 15% (see Extended Data Fig. 9) and extract the phenomenological Ginzburg–Landau superconducting coherence length as $\xi_{GL} = \left(\frac{\Phi_0}{2\pi B_{\perp,c}}\right)^{\frac{1}{2}}$, in which $\Phi_0 = \frac{h}{2e}$ is the superconducting magnetic flux quantum. We note that our coherence length is extracted directly from the critical magnetic field, instead of using the Ginzburg–Landau relation $T_c/T_{c0} = 1 - (2\pi\xi_{GL}{}^2/\Phi_0)B_\perp$ (in which T_{c0} is the mean-field critical temperature at zero magnetic field) and performing a linear fitting near T_c. An analysis of SC1 based on the latter approach will result in an even shorter coherence length and even stronger coupling strength.

Data availability

The data shown in the figures are available from https://doi.org/10.7910/DVN/IADV2O. Other data that support the findings of this study are available from the corresponding author on request.

56. Lu, Z. et al. Extended quantum anomalous Hall states in graphene/hBN moiré superlattices. *Nature* **637**, 1090–1095 (2025).
57. Zhang, F., Sahu, B., Min, H. & MacDonald, A. H. Band structure of ABC-stacked graphene trilayers. *Phys. Rev. B* **82**, 035409 (2010).
58. Yang, J. et al. Spectroscopy signatures of electron correlations in a trilayer graphene/hBN moiré superlattice. *Science* **375**, 1295–1299 (2022).
59. Seiler, A. M. et al. Quantum cascade of correlated phases in trigonally warped bilayer graphene. *Nature* **608**, 298–302 (2022).
60. Cao, Y. et al. Unconventional superconductivity in magic-angle graphene superlattices. *Nature* **556**, 43–50 (2018).
61. Yankowitz, M. et al. Tuning superconductivity in twisted bilayer graphene. *Science* **363**, 1059–1064 (2019).
62. Lu, X. et al. Superconductors, orbital magnets and correlated states in magic-angle bilayer graphene. *Nature* **574**, 653–657 (2019).
63. Chen, G. et al. Signatures of tunable superconductivity in a trilayer graphene moiré superlattice. *Nature* **572**, 215–219 (2019).
64. Zhou, H., Xie, T., Taniguchi, T., Watanabe, K. & Young, A. F. Superconductivity in rhombohedral trilayer graphene. *Nature* **598**, 434–438 (2021).
65. Pantaleón, P. A. et al. Superconductivity and correlated phases in non-twisted bilayer and trilayer graphene. *Nat. Rev. Phys.* **5**, 304–315 (2023).
66. Zhang, Y. et al. Enhanced superconductivity in spin–orbit proximitized bilayer graphene. *Nature* **613**, 268–273 (2023).
67. Holleis, L. et al. Nematicity and orbital depairing in superconducting Bernal bilayer graphene with strong spin orbit coupling. *Nat. Phys.* **21,** 444–450 (2025).
68. Li, C. et al. Tunable superconductivity in electron- and hole-doped Bernal bilayer graphene. *Nature* **631**, 300–306 (2024).
69. Zhang, Y. et al. Twist-programmable superconductivity in spin–orbit-coupled bilayer graphene. *Nature* **641**, 625–631 (2025).
70. Patterson, C. L. et al. Superconductivity and spin canting in spin-orbit-coupled trilayer graphene. *Nature* **641,** 632–638 (2025).
71. Yang, J. et al. Impact of spin-orbit coupling on superconductivity in rhombohedral graphene. *Nat. Mater.* https://doi.org/10.1038/s41563-025-02156-3 (2025).
72. Zhou, H. et al. Isospin magnetism and spin-polarized superconductivity in Bernal bilayer graphene. *Science* **375**, 774–778 (2022).
73. Zhou, H. et al. Half- and quarter-metals in rhombohedral trilayer graphene. *Nature* **598**, 429–433 (2021).
74. Han, T. et al. Orbital multiferroicity in pentalayer rhombohedral graphene. *Nature* **623**, 41–47 (2023).
75. Han, T. et al. Correlated insulator and Chern insulators in pentalayer rhombohedral-stacked graphene. *Nat. Nanotechnol.* **19**, 181–187 (2024).
76. Liu, K. et al. Spontaneous broken-symmetry insulator and metals in tetralayer rhombohedral graphene. *Nat. Nanotechnol.* **19**, 188–195 (2024).
77. Sha, Y. et al. Observation of a Chern insulator in crystalline ABCA-tetralayer graphene with spin-orbit coupling. *Science* **384**, 414–419 (2024).
78. Han, T. et al. Large quantum anomalous Hall effect in spin-orbit proximitized rhombohedral graphene. *Science* **384**, 647–651 (2024).
79. Lu, Z. et al. Fractional quantum anomalous Hall effect in multilayer graphene. *Nature* **626**, 759–764 (2024).
80. Xie, J. et al. Tunable fractional Chern insulators in rhombohedral graphene superlattices. *Nat. Mater.* https://doi.org/10.1038/s41563-025-02225-7 (2025).

Acknowledgements We acknowledge the helpful discussions with S. D. Sarma, J. Sau, X. G. Wen, S. Todadri, F. Zhang, A. Vishwanath, P. Lee, B. Ramshaw, E. A. Kim, A. MacDonald, T. Devakul and A. Young. This study was supported by the US Department of Energy, Office of Science, Basic Energy Sciences, Materials Sciences and Engineering Division under grant no. DE-SC0025325. Device fabrication was performed at the Harvard Center for Nanoscale Systems and MIT.nano. T.H. acknowledges support from a Mathworks Fellowship. L.F. was supported by a Simons Investigator Award from the Simons Foundation. Work in Basel was supported by the EU's H2020 Marie Skłodowska-Curie Actions (MSCA) cofund Quantum Science and Technologies at the European Campus (QUSTEC) grant no. 847471, the Swiss National Science Foundation (grant no. 215757), the Georg H. Endress Foundation and WSS Research Center for Molecular Quantum Systems (molQ) of the Werner Siemens Foundation. K.W. and T.T. acknowledge support from the JSPS KAKENHI (grant nos. 20H00354, 21H05233 and 23H02052) and the World Premier International Research Center Initiative, MEXT, Japan.

Author contributions L.J. supervised the project. T.H. and Z.L. performed the DC magneto-transport measurement. Z. Hadjri, A.A.C., O.S.S., H.W. and D.M.Z. performed some of the in-plane field measurements (Basel). T.H., L.S., Z.W., W.X., Y.Y. and S.Y. fabricated the devices. J.Y., J.S., Z.L. and T.H. helped with installing and testing the dilution refrigerator. T.H. and M.Z. performed the band-structure calculation. H.L., G.S., Z. Hua and P.X. helped with part of the measurements on device T1. K.W. and T.T. grew hBN crystals. L.F. contributed to data analysis. All authors discussed the results and wrote the paper.

Competing interests D.M.Z. is a co-founder of Basel Precision Instruments. The other authors declare no competing interests.

Additional information

Supplementary information The online version contains supplementary material available at https://doi.org/10.1038/s41586-025-09169-7.

Correspondence and requests for materials should be addressed to Long Ju.

Peer review information *Nature* thanks Ying-Ming Xie, Petr Stepanov and the other, anonymous, reviewer(s) for their contribution to the peer review of this work. Peer reviewer reports are available.

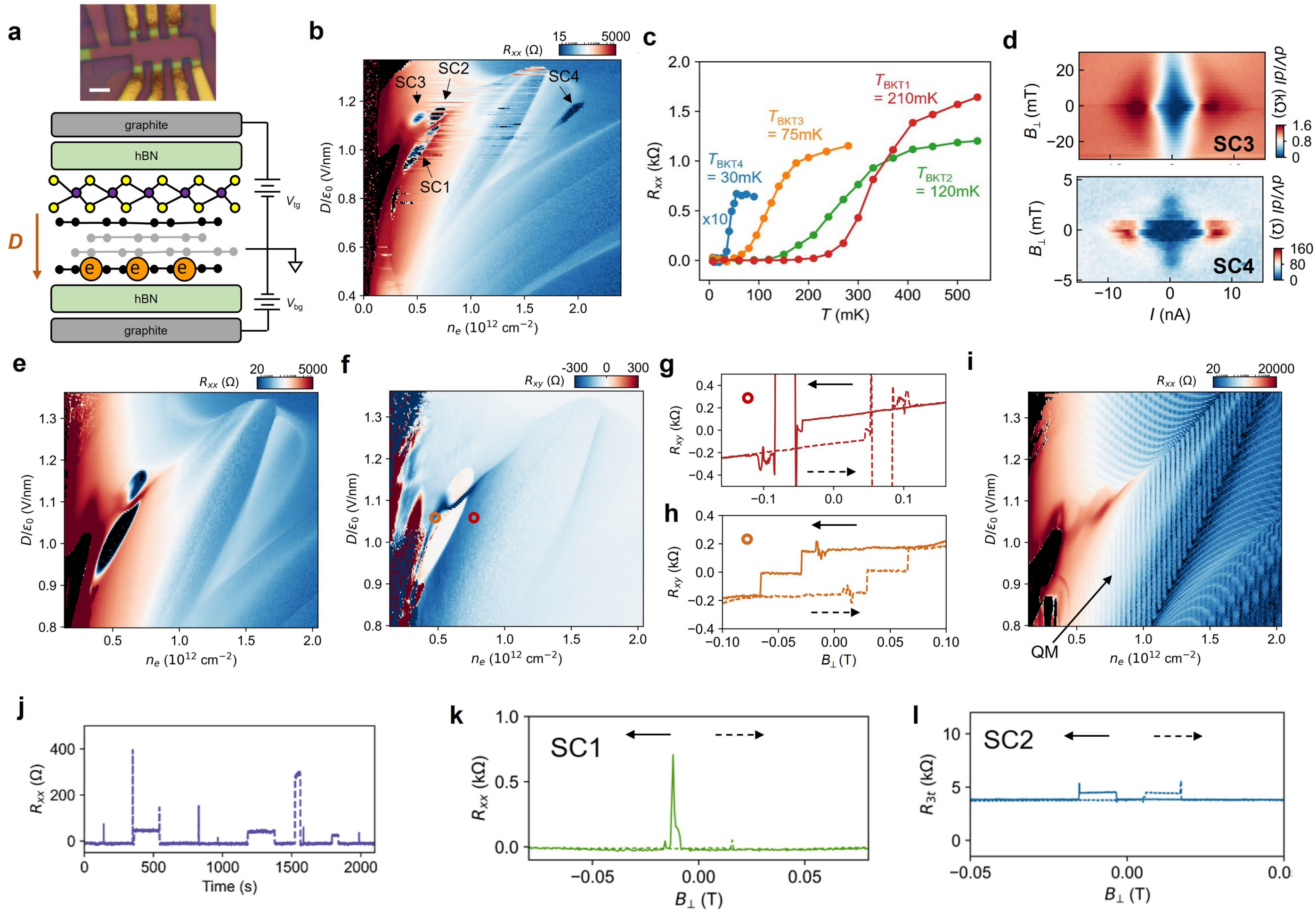

Extended Data Fig. 1 | Superconductivity in rhombohedral tetralayer graphene device T2. a, Optical micrograph and illustration of the structure of rhombohedral tetralayer graphene, in which the electrons are polarized to the layer far away from WSe_2. Scale bar, 3 μm. **b**, Four-terminal resistance R_{xx} as a function of n_e and gate displacement field D/ε_0. Four regions show zero R_{xx} (labelled as SC1–SC4, respectively) and superconductivity. SC1 and SC2 show fluctuations, whereas SC3 and SC4 are smooth. **c**, Temperature dependence of the four superconducting states, with critical temperatures extracted from the comparison of I–V with the BKT model. See Extended Data Fig. 2. **d**, Differential resistance dV_{xx}/dI as a function of current I and out-of-plane magnetic field $B_\perp$ in the SC3 and SC4 states. Both states show peaks of dV/dI as a signature of superconductivity at small magnetic fields. The superconductivity is killed below 30 mT, similar to that of most graphene-based superconductors. **e**,**f**, R_{xx} and R_{xy} maps at 0.1 T, extracted by symmetrizing and antisymmetrizing the data taken at $B_\perp = \pm 0.1$ T. The fluctuations in SC1, SC2 and neighbouring states all disappear. In **f**, SC1 (SC2) is surrounded (neighboured) by states that show anomalous Hall signals. The value of normal Hall signals at the same n_e can be seen in the high-D part of the map. **g**,**h**, Magnetic hysteresis scans of R_{xy} taken at the red and orange circle positions in **d**, showing loops that are consistent with the anomalous Hall signals in **f**. **i**, R_{xx} map taken at $B_\perp = 1.5$ T. The period of quantum oscillations indicates a QM (as labelled by the arrow) that neighbours SC1. Combined with the anomalous Hall signals as shown in **f**, this QM is a spin-polarized and valley-polarized phase. **j**, R_{xx} in SC1 (at $n_e = 0.55 \times 10^{12}$ cm^{-2} and $D/\varepsilon_0 = 1.02$ V nm^{-1}) as a function of time, featuring fluctuations when gate voltages are fixed. **k**,**l**, Representative magnetic hysteresis of R_{xx} taken in SC1 (at $n_e = 0.57 \times 10^{12}$ cm^{-2} and $D/\varepsilon_0 = 1.05$ V nm^{-1}) and SC2 (at $n_e = 0.7 \times 10^{12}$ cm^{-2} and $D/\varepsilon_0 = 1.16$ V nm^{-1}). We note that one of the four terminals was damaged during measurement, resulting in only three-terminal resistance measurement being possible.

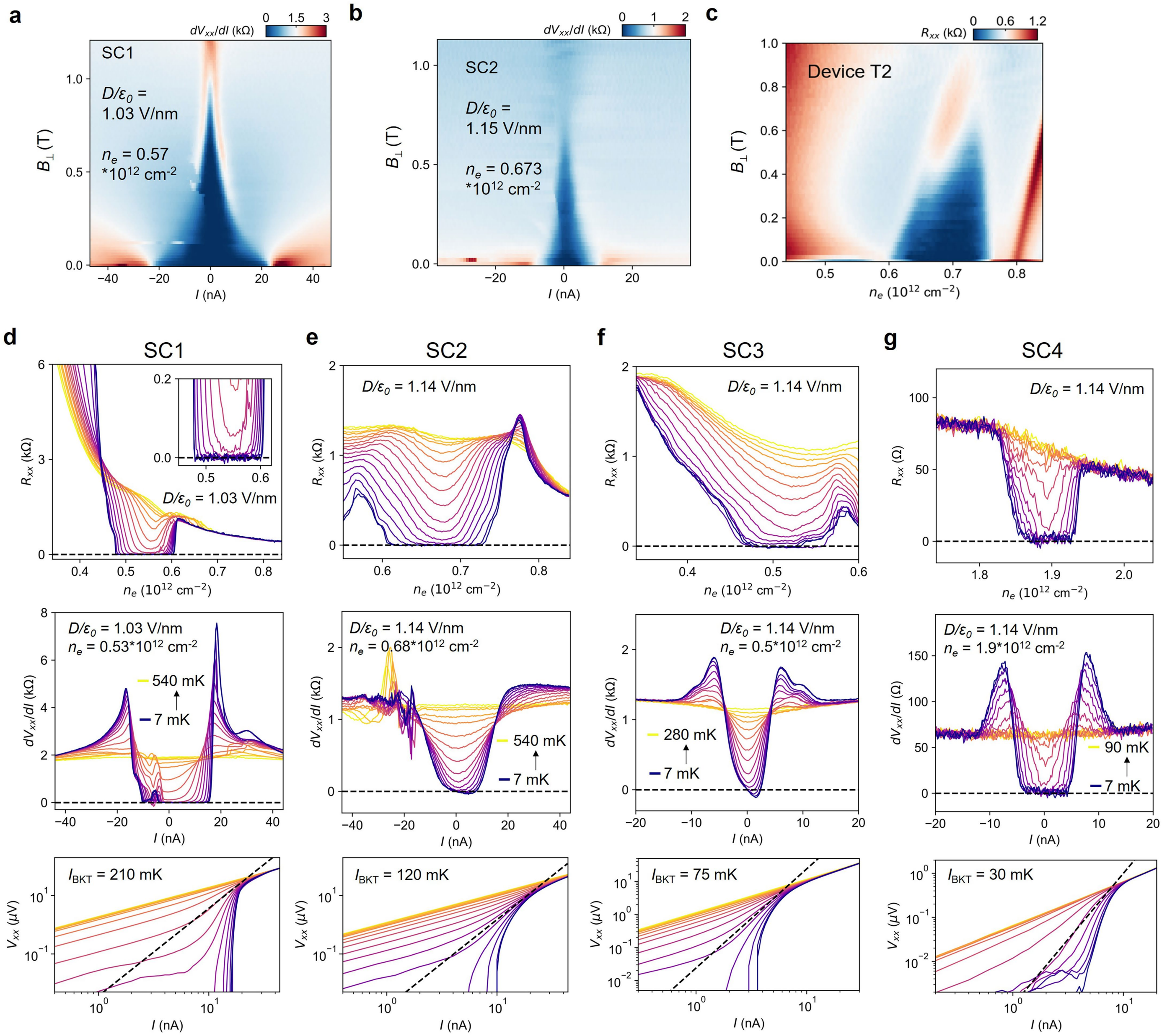

Extended Data Fig. 2 | Detailed characterizations of SC1–SC4 in device T2. **a**,**b**, Differential resistance dV_{xx}/dI versus I and $B_\perp$ for SC1 and SC2 in device T2, respectively. The vanishing differential resistance persists to about 1 T and about 0.6 T in SC1 and SC2, respectively. **c**, B–n_e map at D/ε_0 = 1.14 V nm^{-1}. **d**–**g**, Temperature dependence of longitudinal and differential resistances and BKT fitting for SC1–SC4. These are taken at representative (n_e, D) combinations corresponding to Extended Data Fig. 1c. Panels in the same column correspond to a specific superconducting state. Zero resistance, differential resistance peak at critical current and the BKT scaling ($V_{xx} \propto I^3$, as indicated by the dashed lines in the lower panels) can be seen for all four of the superconducting states.

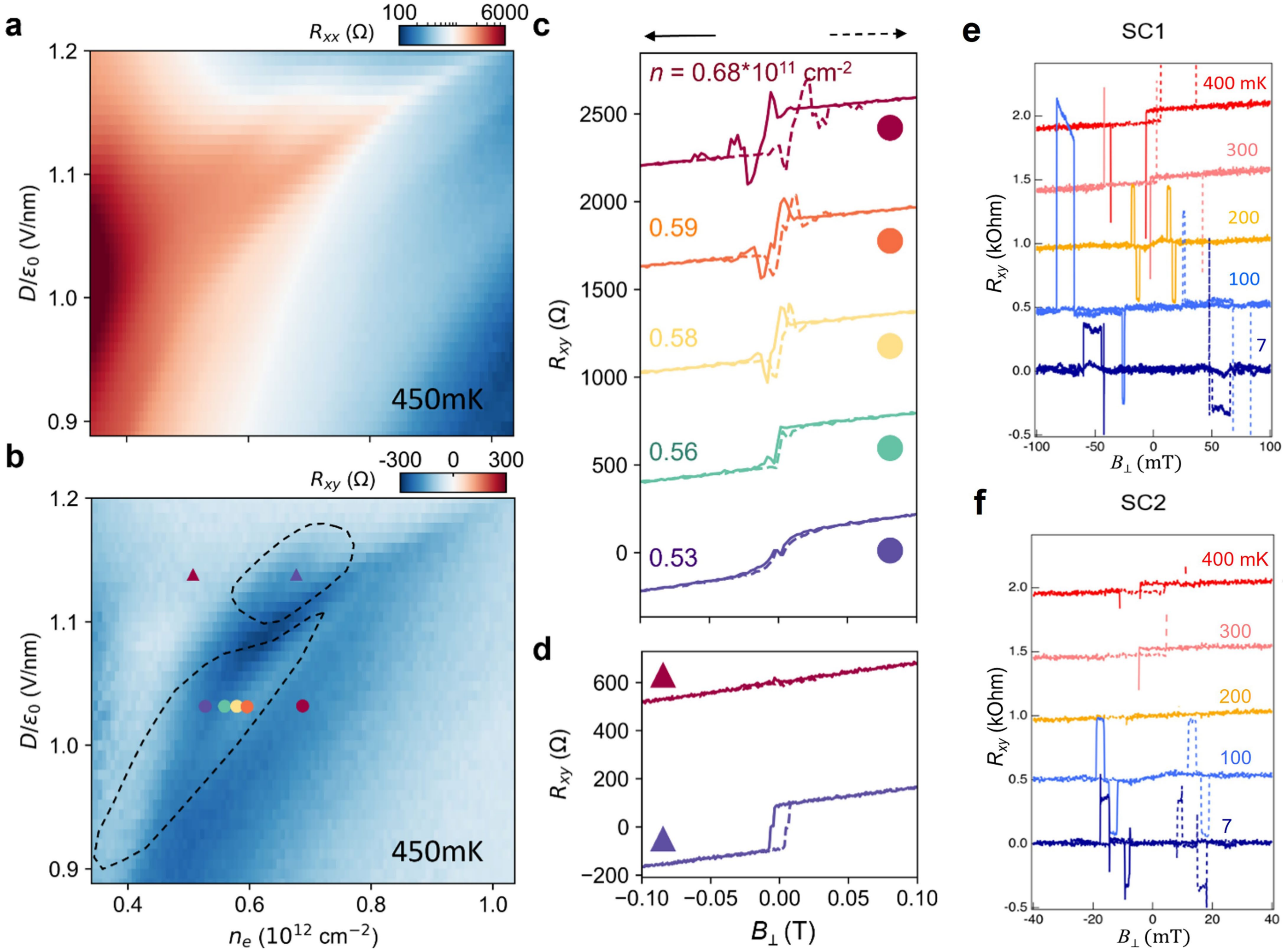

Extended Data Fig. 3 | Anomalous Hall effects and TRSB in the normal state of SC1 and SC2 in device T2. a,**b**, Symmetrized R_{xx} and antisymmetrized R_{xy} map at 0.1 T and 450 mK, above the critical temperatures of SC1 and SC2. The dashed curves in **b** outline the boundary of SC1 and SC2, inside which clear anomalous Hall signals can be seen in the normal states. **c**,**d**, Magnetic hysteresis scans at the dot and triangle positions in **b**. Clear hysteresis loops can be seen in both the states surrounding SC1, as well as in SC1 and SC2. **e**,**f**, Temperature-dependent antisymmetrized R_{xy} hysteresis at a state in SC1 and SC2, respectively. Curves are shifted vertically for clarity.

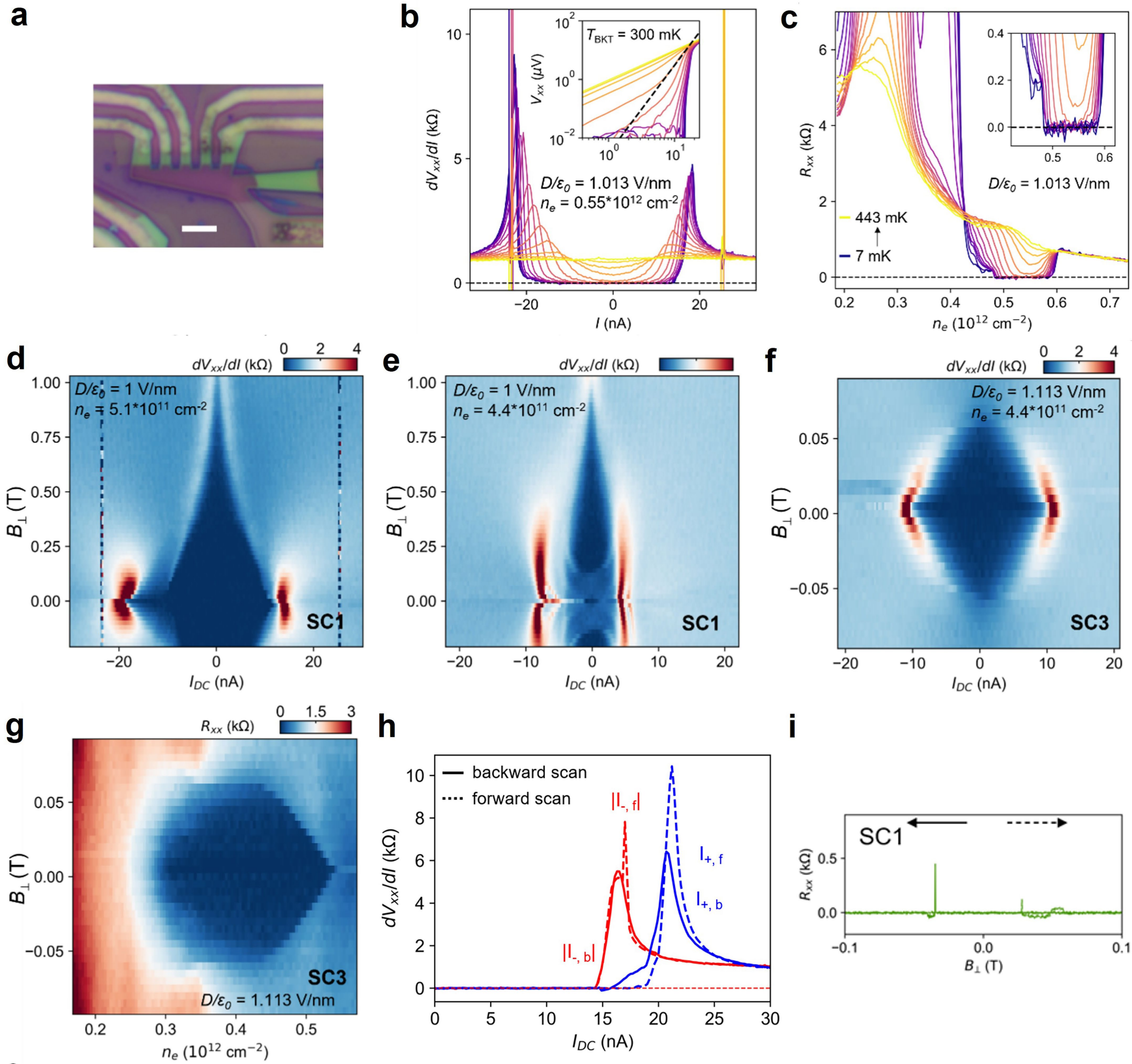

Extended Data Fig. 4 | Superconductivities in device T3. a, Optical micrograph of the device. Scale bar, 3 µm. **b**, Temperature-dependent differential resistance dV_{xx}/dI versus I at a typical (n_e, D) inside the SC1 region, featuring zero resistance at low current and a pair of peaks at critical current. **c**, Temperature-dependent R_{xx} at a constant D, featuring a density range of zero resistance that corresponds to SC1. **d**–**f**, Differential resistance at typical n_e–D positions inside SC1 and SC3. The vanishing differential resistance persists to about 1 T for SC1, whereas that of SC3 persists to only about 50 mT. **g**, R_{xx} as a function of n_e and $B_\perp$ at D/ε_0 = 1.113 V nm^{-1} in SC3. The density range corresponding to SC3 continues shrinking on $B_\perp$. **h**, Differential resistance measurement in SC1, showing the superconducting diode effect. **i**, Representative magnetic hysteresis of R_{xx} taken in SC1 (at $n_e = 0.5 \times 10^{12}$ cm^{-2} and D/ε_0 = 0.985 V nm^{-1}).

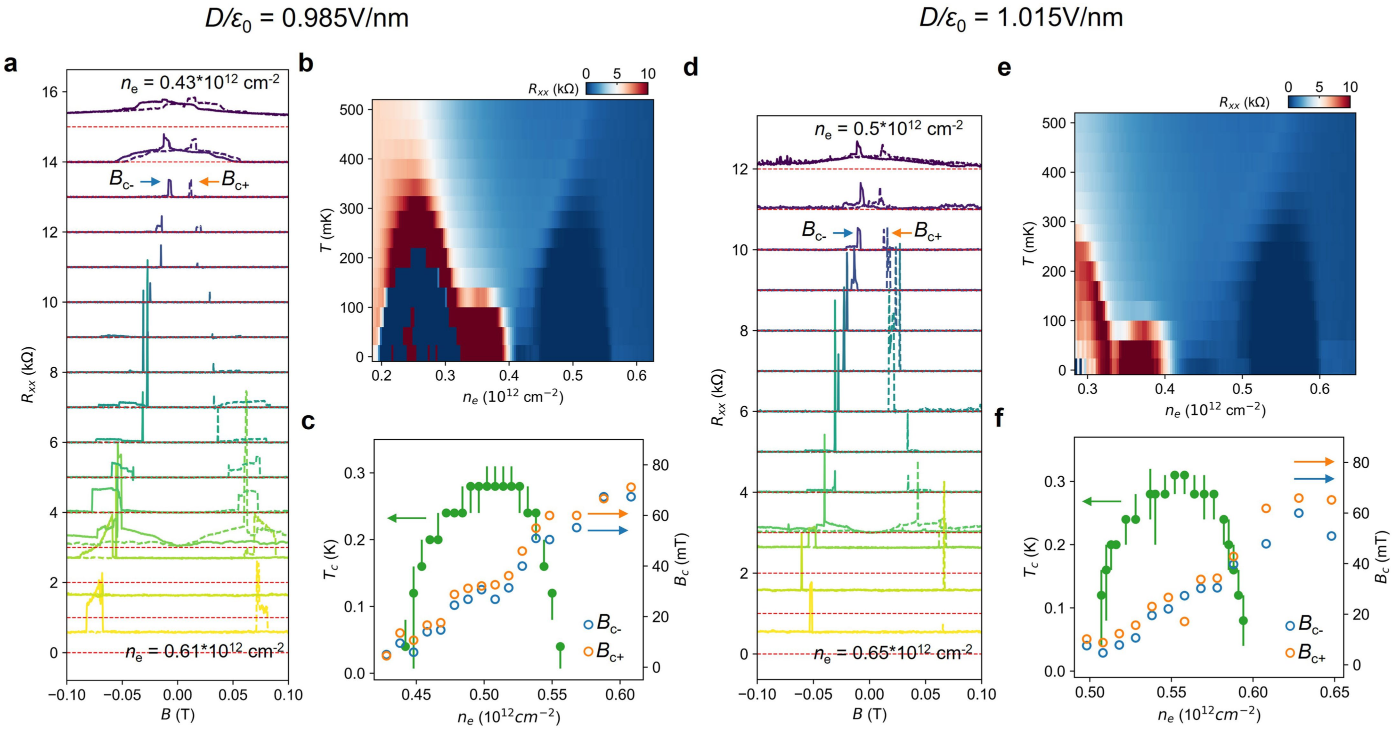

Extended Data Fig. 5 | Magnetic hysteresis, coercive field and superconducting critical temperature in SC1 in device T3. a, R_{xx} as a function of the out-of-plane magnetic field at different n_e and D/ε_0 = 0.985 V nm^{-1}. The curves are shifted vertically for clarity. The dashed horizontal lines indicate the shift of each curve (which corresponds to zero resistance). Orange and blue arrows indicate the coercive fields, which is defined as the closest-to-zero magnetic field, in which R_{xx} increases rapidly. **b**, Colour map of R_{xx} versus T and n_e. **c**, Summary of the coercive fields and the superconducting T_c at different n_e and D/ε_0 = 0.985 V nm^{-1}. **d**–**f**, Same as **a**–**c** but for D/ε_0 = 1.015 V nm^{-1}.

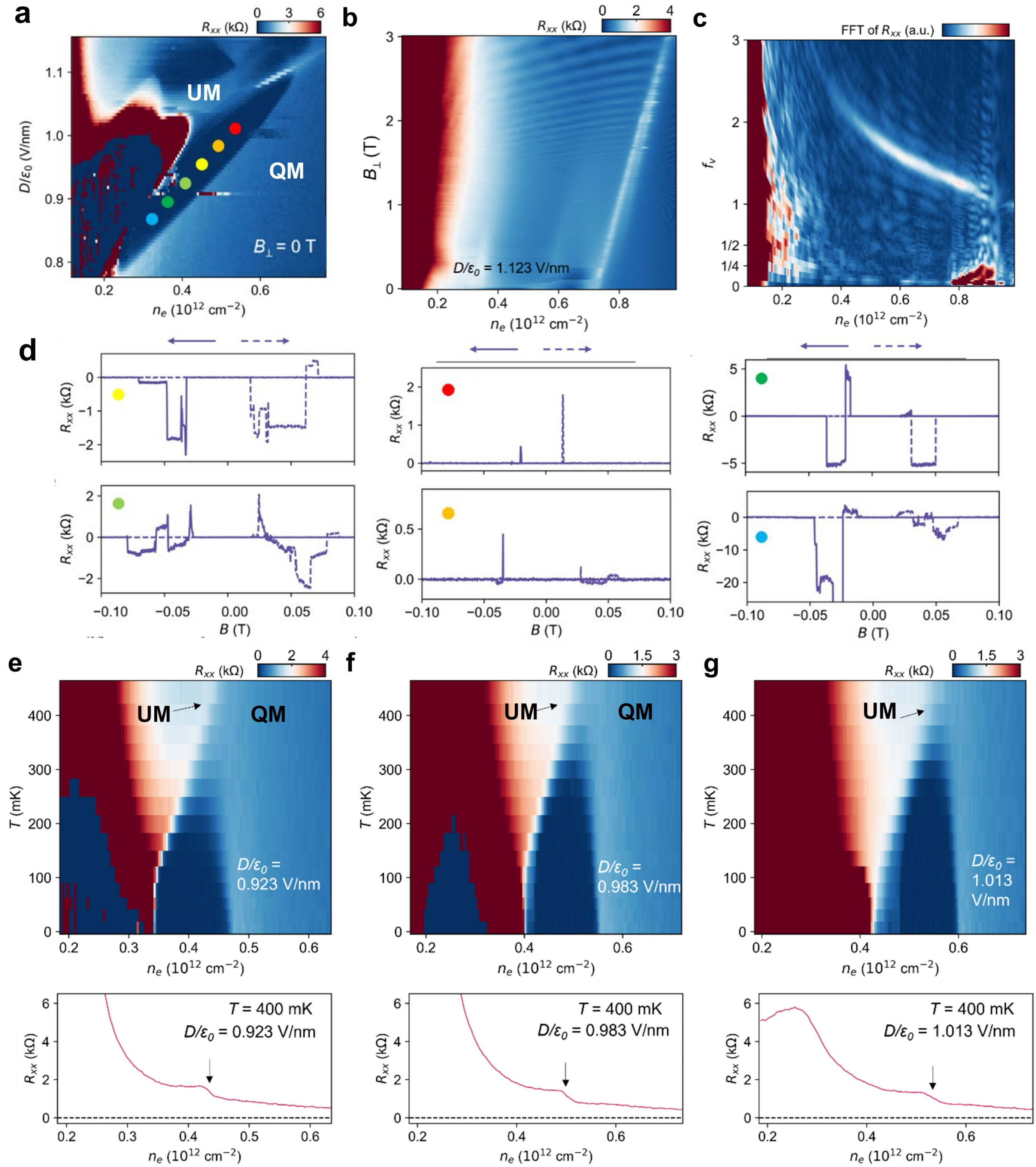

Extended Data Fig. 6 | Magnetic hysteresis, quantum oscillations and temperature dependence of SC1 in device T3. a, The n_e–D map of R_{xx} taken at zero magnetic field in device T3. **b**, Landau fan diagram taken at $D/\varepsilon_0 = 1.123$ V nm^{-1}, revealing quantum oscillations starting at $B_\perp \approx 1.5$ T. **c**, Fast Fourier transform spectra of data in **b**. A diagonal feature above $f_v = 1$ suggests a QM state with annular Fermi surface. However, the low-frequency component of this annular Fermi-surfaced metal is not clear from the data. **d**, Out-of-plane magnetic field scans of R_{xx} at different (n_e, D) indicated by the coloured dots in **a**. Magnetic hysteresis was observed across a large range of (n_e, D) parameter space across SC1. **e**–**g**, Upper panels, R_{xx} as a function of T and n_e at three displacement fields cutting through SC1. In all cases, there is a clear boundary as indicated by the black arrow at above T_c. This boundary shifts to lower n_e values as the temperature is lowered. Superconductivity domes emerge within the phase to the right of this boundary, suggesting that this phase to the right (the spin-polarized and valley-polarized QM) is the parent state of SC1. Lower panels, linecuts at $T = 400$ mK from the upper panels, featuring kinks that correspond to the phase boundary between the spin-polarized and valley-polarized QM and the metal state at lower densities.

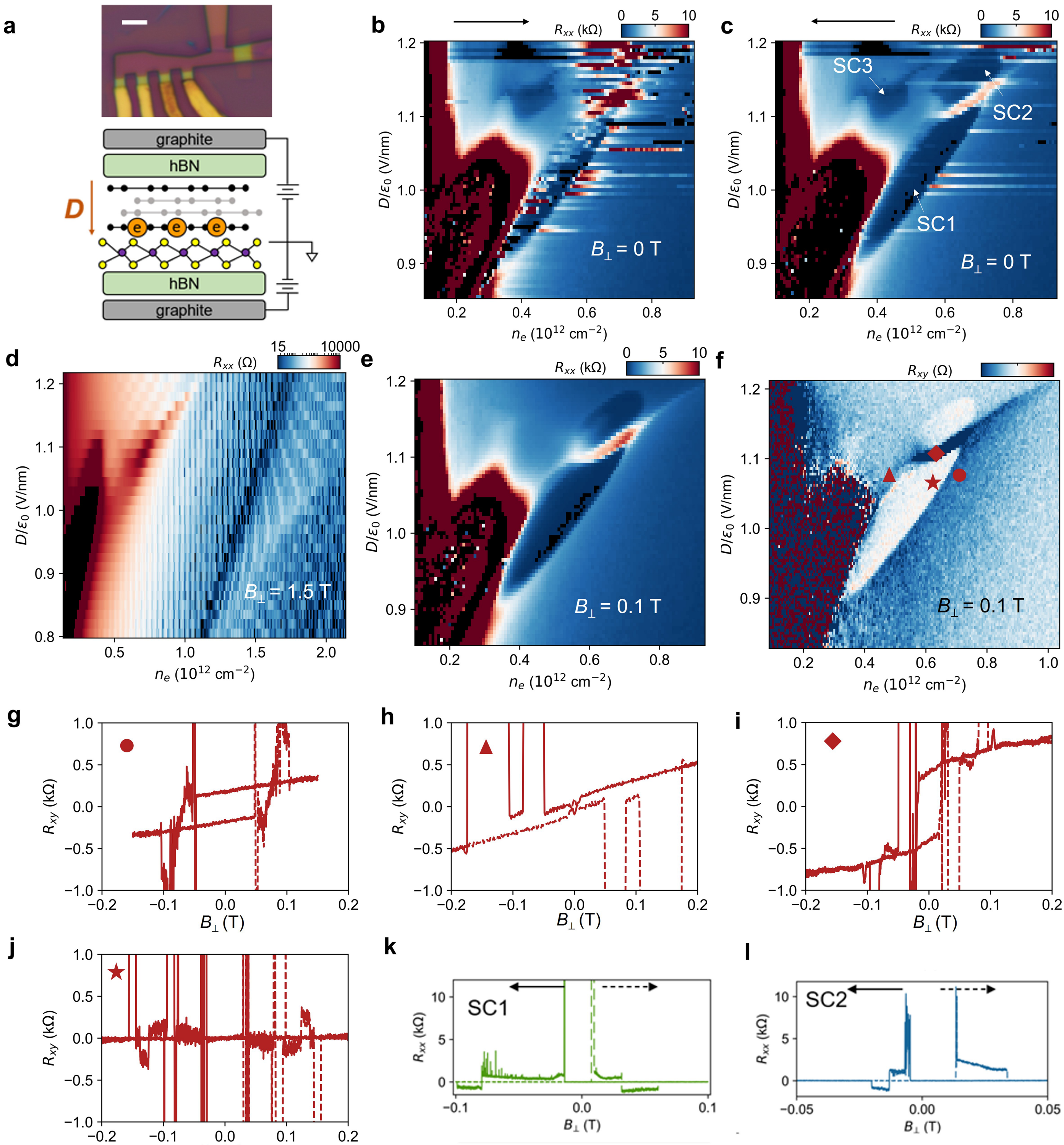

Extended Data Fig. 7 | Superconductivities in device T1. a, Optical micrograph and device configuration, in which electrons are polarized to the bottom layer of tetralayer graphene with WSe_2 at proximity. Scale bar, 3 μm. **b**,**c**, The n_e–D maps of R_{xx} at $B_\perp$ = 0 T and base temperature, corresponding to opposite sweeping directions of n_e, respectively. Three superconducting regions labelled as SC1–SC3 similar to in devices T2 and T3 can be seen. Some fluctuations can be seen in SC1, SC2 and the neighbouring metallic region. **d**, The n_e–D map of R_{xx} at $B_\perp$ = 1.5 T and base temperature, featuring the quantum oscillations of a QM to the right of the SC1 region. **e**,**f**, The n_e–D map of R_{xx} and R_{xy} at $B_\perp$ = 0.1 T and base temperature. The fluctuations and SC3 are both suppressed, similar to those observed in device T2. **g**–**j**, Magnetic hysteresis scans of R_{xy} taken at the dot, triangle, diamond and star positions in **f**, showing jumps/loops that are consistent with the anomalous Hall signals in **f**. **k**,**l**, Representative magnetic hysteresis of R_{xx} taken in SC1 (at $n_e = 0.54 \times 10^{12}$ cm^{-2} and D/ε_0 = 1.03 V nm^{-1}) and SC2 (at $n_e = 0.72 \times 10^{12}$ cm^{-2} and D/ε_0 = 1.17 V nm^{-1}).

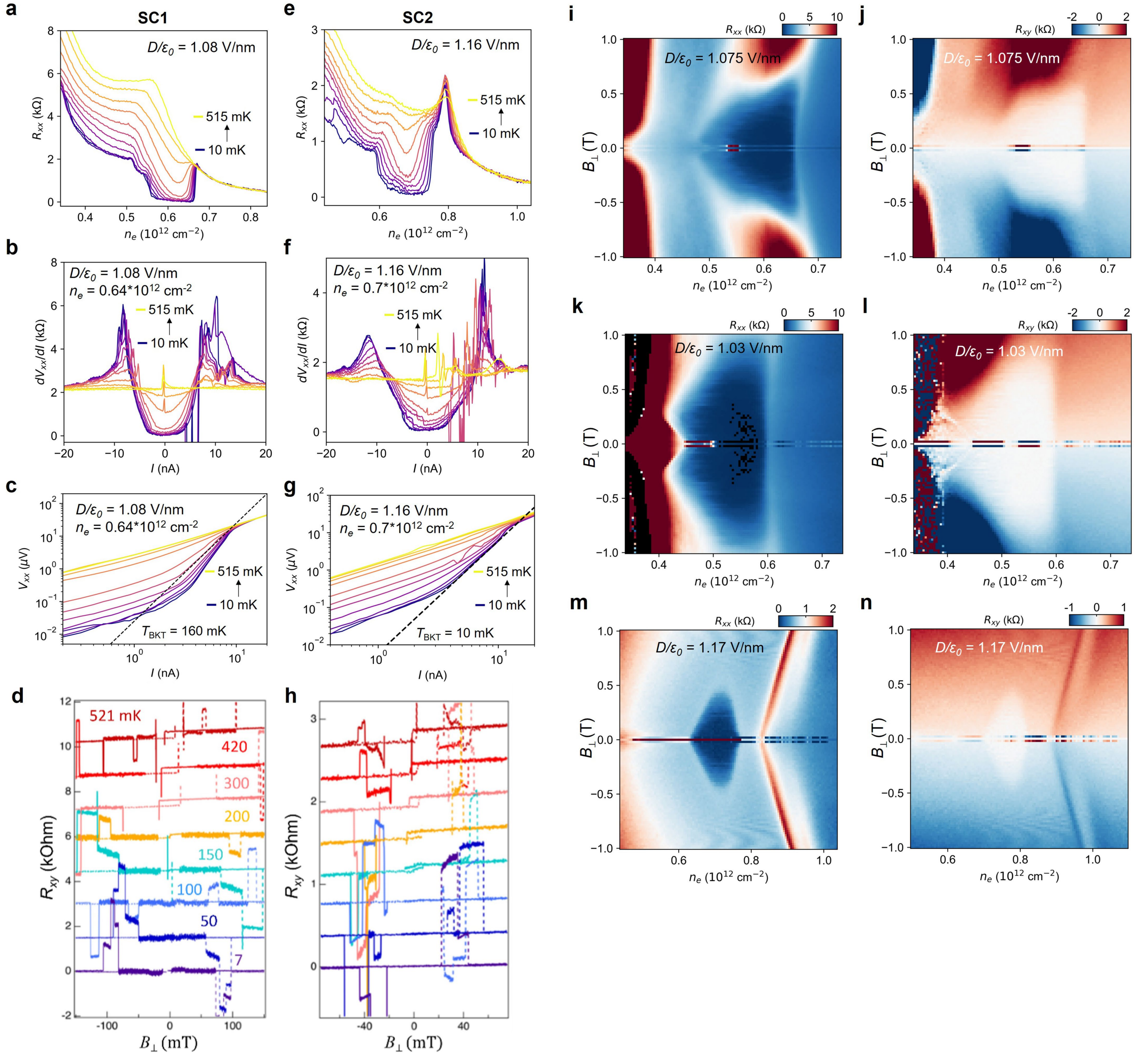

Extended Data Fig. 8 | Temperature and magnetic field dependence of superconductivity in device T1. **a**–**c**, Temperature dependence of R_{xx}, the difference resistance dV_{xx}/dI versus I and the BKT fitting of SC1, respectively. **d**, Temperature-dependent antisymmetrized R_{xy} hysteresis at a state in SC1. **e**–**g**, Temperature dependence of R_{xx}, the difference resistance dV/dI versus I and the BKT fitting of SC2, respectively. **h**, Temperature-dependent antisymmetrized R_{xy} hysteresis at a state in SC2. **i**,**j**, R_{xx} and R_{xy} as a function of n_e and $B_\perp$ at $D/\varepsilon_0 = 1.075$ V nm^{-1} (corresponding to SC1), respectively. The phase boundary between the QM and SC1 remains at the same n_e, indicating that the orbital magnetism is continuous across the boundary and SC1 is orbital magnetic. **k**,**l**, R_{xx} and R_{xy} as a function of n_e and $B_\perp$ at $D/\varepsilon_0 = 1.03$ V nm^{-1} (corresponding to SC1), respectively. The phase boundary between the QM and SC1 remains at the same n_e, whereas the left boundary of SC1 even moves against the neighbouring state in magnetic field, confirming the orbital magnetic nature of SC1. **m**,**n**, R_{xx} and R_{xy} as a function of n_e and $B_\perp$ at $D/\varepsilon_0 = 1.17$ V nm^{-1} (corresponding to SC2), respectively. The phase boundaries between SC2 and neighbouring states move towards SC2 under magnetic field.

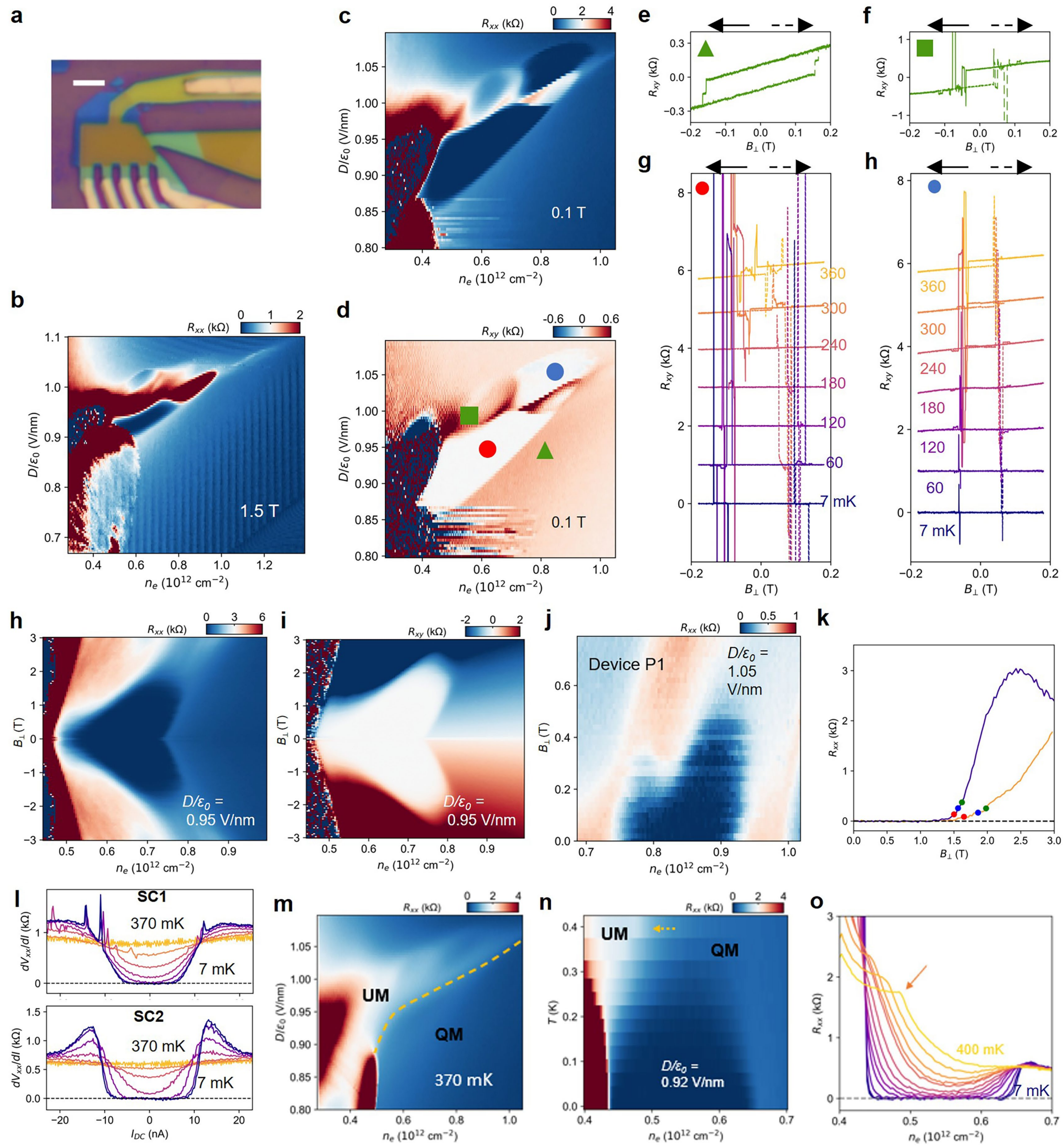

Extended Data Fig. 9 | Superconductivities in device P1. a, Optical micrograph of the device. Scale bar, 3 µm. **b**, The n_e–D map of R_{xx} at $B_\perp = 1.5$ T and base temperature, featuring the quantum oscillations corresponding to the QM state neighbouring SC1. **c**,**d**, The n_e–D map of R_{xx} and R_{xy} at $B_\perp = 0.1$ T and base temperature, respectively. **e**,**f**, Magnetic hysteresis of R_{xy} at the green triangle and square positions in **d**. **g**,**h**, Temperature dependence of antisymmetrized R_{xy} in SC1 (corresponding to the red dot position in **d**) and SC2 (corresponding to the blue dot position in **d**), respectively. Curves are shifted vertically for clarity. **h**,**i**, R_{xx} and R_{xy} as a function of n_e and $B_\perp$ at $D/\varepsilon_0 = 0.955$ V nm^{-1}, respectively. The phase boundary between the QM and SC1 shifts to slightly higher density, suggesting the orbital magnetic nature of SC1. **j**, The n_e–B map of R_{xx} at $D/\varepsilon_0 =$ 1.05 V nm^{-1}, cutting through SC2. **k**, Magnetic field dependence of R_{xx} in two representative states inside SC1. We use 10% (indicated by the blue dots) of the normal state resistance to extract the T_c and 5% (red dots) and 15% (green dots) of the normal state resistance to extract the uncertainty of T_c in Fig. 5. **l**, dV_{xx}/dI versus I in SC1 and SC2 at (0.61×10^{12} cm^{-2}, 0.94 V nm^{-1}) and (0.85×10^{12} cm^{-2}, 1.05 V nm^{-1}), respectively, featuring zero resistance at small current and the resistance spikes at critical current. **m**, The n_e–D map of R_{xx}, highlighting (by the orange dashed curve) the phase boundary between the spin-polarized and valley-polarized QM and an UM. **n**, Temperature-dependent R_{xx} linecut at $D/\varepsilon_0 = 0.92$ V nm^{-1}, in which the QM–UM phase boundary (indicated by the orange dashed arrow) gradually shifts as T is lowered. The SC1 state develops to the right of the boundary, indicating the QM as the parent state of SC1. **o**, Linecuts from **n**, showing the QM–UM phase boundary as a kink (orange arrow) in R_{xx}, which shifts to lower n_e as T is lowered.

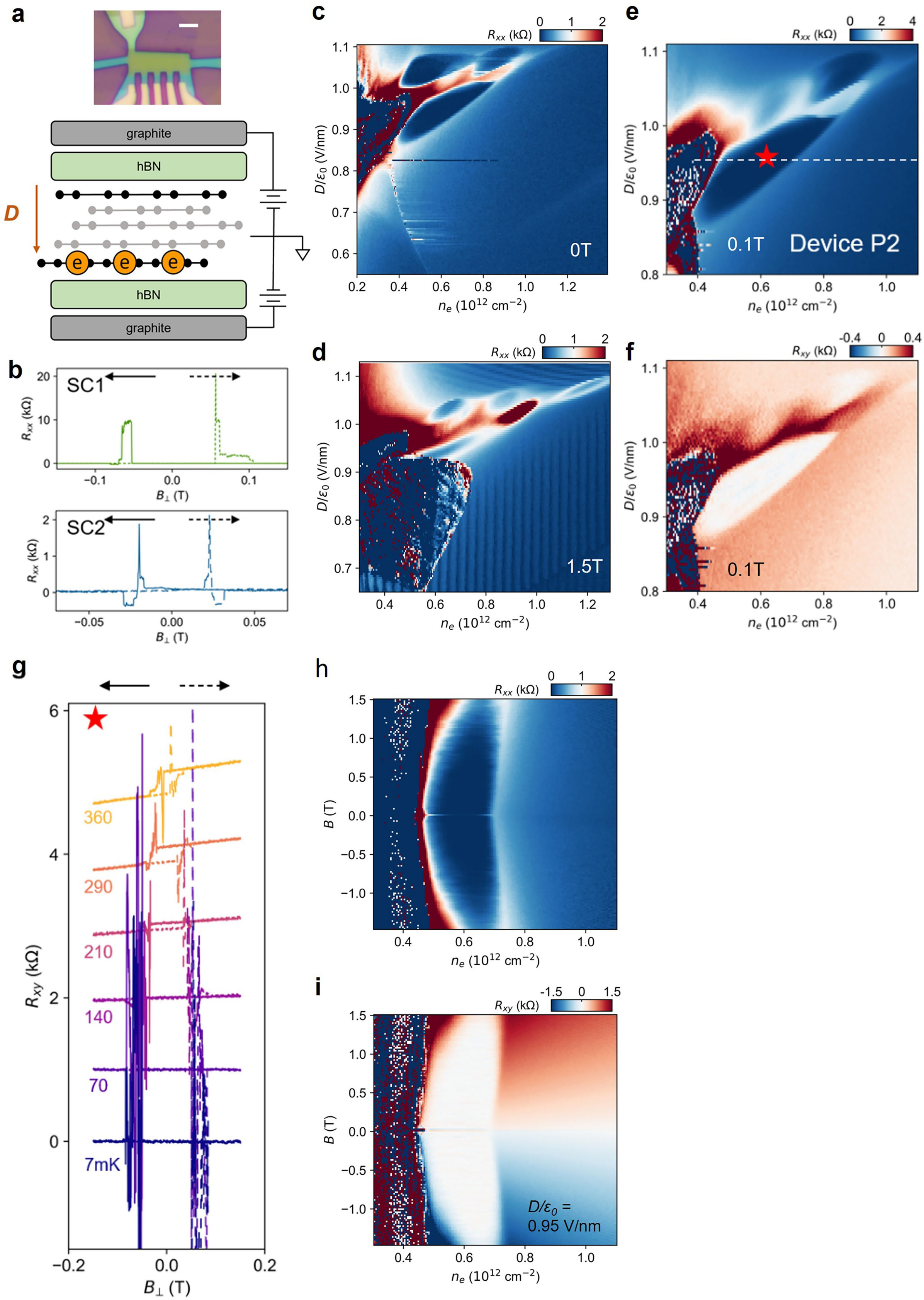

Extended Data Fig. 10 | Superconductivities in device P2. **a**, Optical micrograph and illustration of the device configuration. Scale bar, 3 μm. **b**, Magnetic hysteresis in SC1 (at $n_e = 0.61 \times 10^{12}$ cm^{-2} and $D/\varepsilon_0 = 0.95$ V nm^{-1}) and SC2 (at $n_e = 0.87 \times 10^{12}$ cm^{-2} and $D/\varepsilon_0 = 1.07$ V nm^{-1}) at base temperature, respectively. **c**, The n_e–D map of R_{xx} at zero magnetic field, featuring SC1–SC3. **d**, The n_e–D map of R_{xx} at $B_\perp = 1.5$ T, featuring the QM state to the higher density side of SC1. **e**,**f**, The n_e–D map of R_{xx} and R_{xy} at $B_\perp = 0.1$ T and base temperature. **g**, Temperature-dependent magnetic hysteresis of R_{xy} at the star position in **e**. Curves are shifted vertically for clarity. **h**,**i**, R_{xx} and R_{xy} as a function of n_e and $B_\perp$ along the dashed line in **e**, respectively. The phase boundary between the QM and SC1 shifts to slightly higher density, suggesting the orbital magnetic nature of SC1.

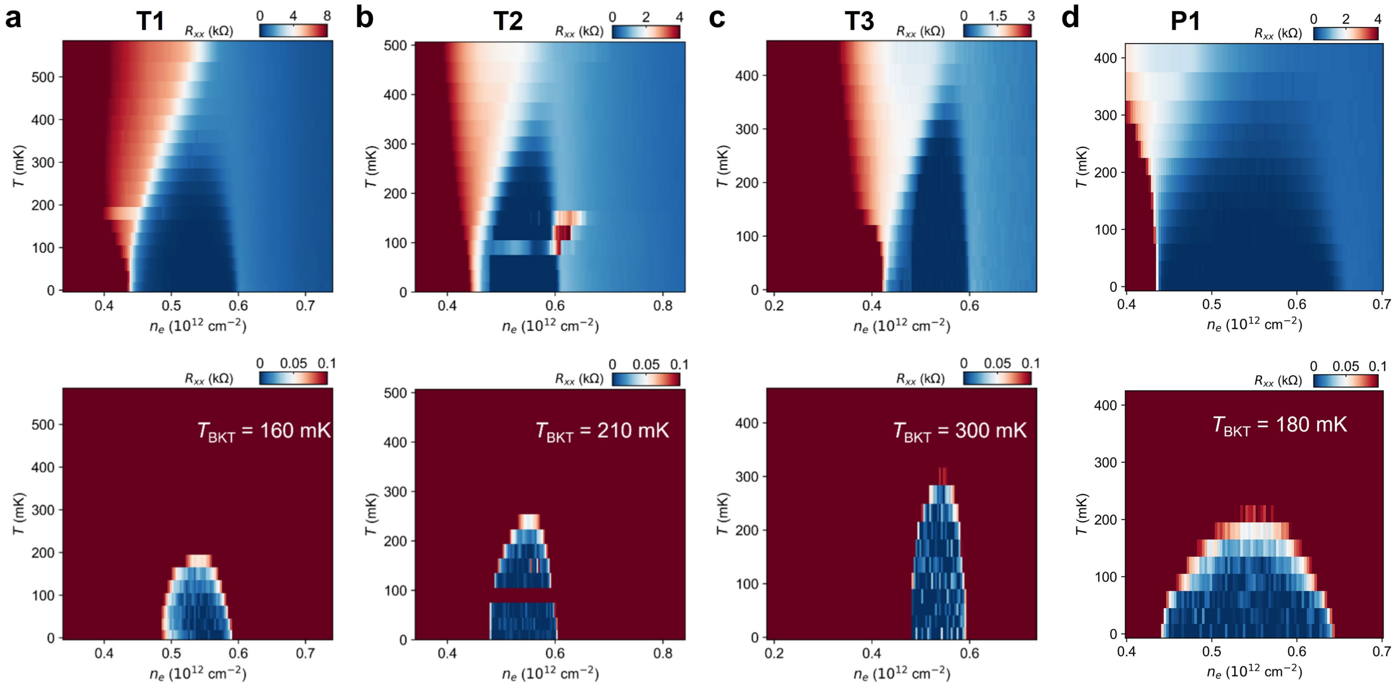

Extended Data Fig. 11 | Comparison between the highest superconducting transition temperatures of SC1 in devices T1–T3 and P1. a–**d**, Upper panels, R_{xx} as a function of temperature and charge density at a constant D that corresponds to the highest T_c, in the four devices, respectively. Lower panels, the same plots as in the upper panels with a small unified colour scale for a fair comparison. The BKT fitting reveals an increase of T_{BKT} from device T1 to T3, corresponding to a weakening of spin–orbit-coupling effect.

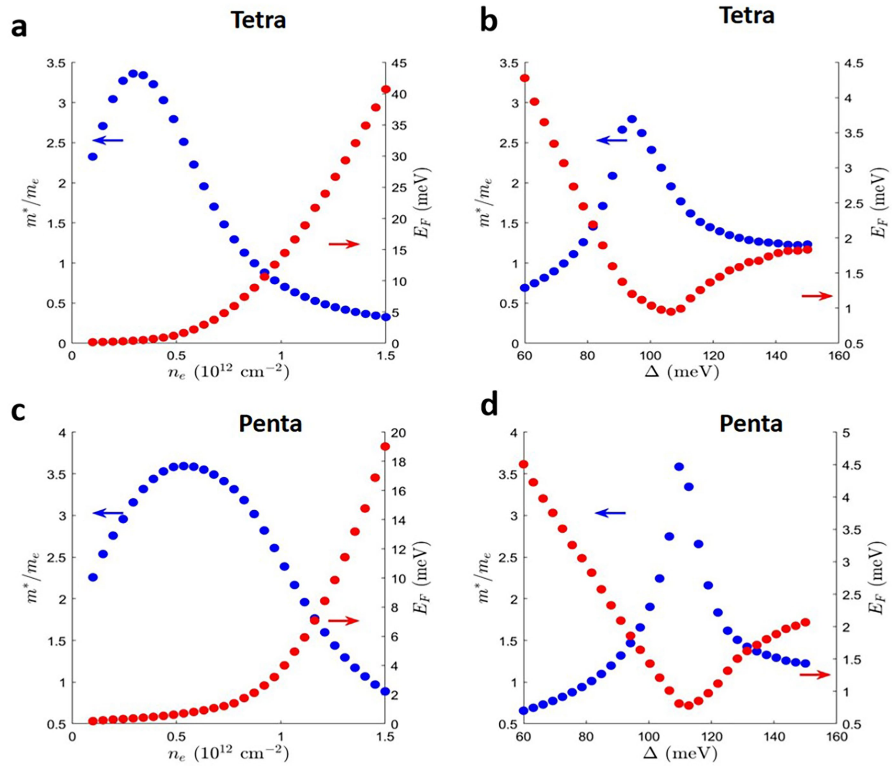

Extended Data Fig. 12 | Calculation of the effective mass and Fermi energy in tetralayer and pentalayer rhombohedral graphene. a, Calculation at a fixed potential difference between the top-most and bottom-most layers $\Delta = 90$ meV in tetralayer graphene. **b**, Calculation at a fixed charge density $n_e = 0.5 \times 10^{12}$ cm^{-2} in tetralayer graphene. **c**, Calculation at a fixed potential difference $\Delta = 110$ meV in pentalayer graphene. **d**, Calculation at a fixed charge density $n_e = 0.6 \times 10^{12}$ cm^{-2} in pentalayer graphene.